Article:
Germa, A, Koebli, D, Wetmore, P et al. (6 more authors) (2020) Crystallization and Segregation of Syenite in Shallow Mafic Sills: Insights from the San Rafael Subvolcanic Field, Utah. Journal of Petrology, 61 (9). ISSN 0022-3530

https://doi.org/10.1093/petrology/egaa092

Crystallization and segregation of syenite in shallow mafic sills: insights from the San Rafael subvolcanic field, Utah.

Aurelie Germa, School of Geosciences, University of South Florida, 4202 E Fowler Avenue, Tampa, FL 33620, USA

Danielle Koebli, School of Geosciences, University of South Florida, 4202 E Fowler Avenue, Tampa, FL 33620, USA

Paul Wetmore, School of Geosciences, University of South Florida, 4202 E Fowler Avenue, Tampa, FL 33620, USA

Zachary Atlas, School of Geosciences, University of South Florida, 4202 E Fowler Avenue, Tampa, FL 33620, USA

Austin Arias, School of Earth and Environmental Sciences, Seoul National University, Gwanak-ro 1, Gwanak-gu, Seoul, Republic of Korea

Ivan P. Savov, School of Earth and Environment, Institute of Tectonics and Geophysics, University of Leeds, Leeds LS2 9JT, United Kingdom

Mikel Diez, School of Mathematics, University of Bristol, Bristol BS8 1TH, United Kingdom

Vanessa Greaves, School of Earth and Environment, University of Leeds, Leeds LS2 9JT, United Kingdom

Elisabeth Gallant, Department of Geography, University of Cambridge, 20 Downing Pl, Cambridge CB2 1QB

Corresponding author: agerma@usf.edu

KEYWORDS

Crystallization, Monogenetic volcanism, Plumbing system, San Rafael subvolcanic field, Sill, Dike, Conduit, Syenite, Thermobarometry

ABSTRACT

Exposed plumbing systems provide important insight into crystallization and differentiation in shallow sills beneath volcanic fields. We use whole rock major element, trace element, and radiogenic isotopic compositions, along with mineral geochemical data on 125 samples to examine the conditions of melt differentiation in shallow sills from the exposed 4-Ma-old San Rafael subvolcanic field (SRVF), Utah. The field consists of ~2,000 dikes, 12 sills, and 63 well preserved volcanic conduits. Intrusive rocks consist of mainly fine-grained trachybasalts and coarse-grained syenites; which are alkaline, comagmatic, and enriched in Ba, Sr and LREE. Within sills, syenite is found as veins, lenses, and sheets totally enveloped by the basalt. The SRVF intrusions have geochemical signatures of both enriched sub-continental lithospheric and asthenospheric mantle sources. We estimate partial melting occurred between 1.2 and 1.9 GPa (50 - 70 km), with mantle potential temperatures in the range 1260 - 1326 ± 25°C, consistent with those estimated for volcanic rocks erupted on the Colorado Plateau. Geobarometry results based on clinopyroxene chemistry indicate that (1) basalt crystallized during ascent from at least 40 km deep with limited lithospheric storage, and (2) syenites crystallized only in the sills, ~1 km below the surface. San Rafael mafic magma emplaced in sills and started to crystallize inward from the sill margins. Densities of basalt and syenite at solidus temperatures are 2.6 and

2.4 g/cc, respectively, with similar viscosities of ~150 Pa s. Petrographic observations and physical properties suggest that syenite can be physically separated from basalt by crystal compaction and segregation of the tephrophonolitic residual liquid out of the basaltic crystal mush after reaching 30-45 % of crystallization. Each individual sill is 10– 50 m thick and would have solidified fairly rapidly (1-30 years), the same order of magnitude as the duration of common monogenetic eruptions. Our estimates imply that differentiation in individual shallow sills may occur during the course of an eruption whose style may vary from effusive to explosive by tapping different magma compositions. Our study shows that basaltic magmas have the potential to differentiate to volatile-rich magma in shallow intrusive systems, which may increase explosivity.

INTRODUCTION

Understanding petrogenetic processes that occur in subvolcanic systems, emplaced at shallow depth (down to ~3 km; Rocchi & Breitkreuz, 2017), is a major challenge in geosciences. Processes that occur in shallow plumbing systems prior to and during volcanic eruptions directly influence eruptive style. During the course of a single eruption, eruptive dynamics can vary from effusive through slightly explosive (fountaining, Hawaiian), to Strombolian and phreatomagmatic explosions (Valentine & Gregg, 2008; Harp & Valentine, 2015). Eruptive style and duration also vary according to the volume and geometry of conduits and shallow sills, especially when magma is being focused from an initial fissure to a conduit (Keating et al., 2008; Genareau et al., 2010; Valentine & Cortés, 2013). However, the physical processes occurring in the subsurface are not directly observable at volcanic fields. Fortunately, we can investigate shallow magmatic plumbing systems at highly eroded volcanic fields where networks of dikes, sills, and conduits are exposed (Keating et al., 2008; Lefebvre et al., 2012). Such volcanic fields provide an exceptional opportunity to study geochemical and petrological changes that occur in shallow magma storage regions, e.g., sills, where *in situ* crystallization and differentiation may operate - processes that may create evolved melts that are segregated from the basaltic parent (Carman, 1994; Caroff et al., 1997; Marsh, 2002; Zavala et al., 2011; Masotta et al., 2012). Such melts, stored in sills, may be remobilized in the event of the transition from storage to feeder dike and conduit to potentially trigger explosive eruptions. The results of this and similar studies of subvolcanic plumbing systems should serve to ground real-time interpretations made from remote (i.e. magnetic, geodetic, and seismic) signals during eruptions by identifying and placing constraints on rates and magnitudes of the various magmatic processes occurring in these shallow systems.

Magma plumbing systems have been traditionally described as simple *straw and balloon* models, but variable and more complex structures, mostly networks of multiple magma storage units like dikes, sills, conduits, and sheets, are now more generally accepted (Cartwright & Hansen, 2006; Harp & Valentine, 2015; Burchardt & Galland, 2016; Jerram & Bryan, 2017). Studies on partially to highly eroded monogenetic volcanic fields in the Southwest US confirm the presence of shallow plumbing systems in the form of dikes, sills, and conduits beneath monogenetic volcanoes (Tingey et al., 1991; Delaney & Gartner, 1997; Hintz & Valentine, 2012; Harp & Valentine, 2015; Muirhead et al., 2016). Variable geochemical signatures are obvious at polygenetic volcanoes, but only recently studied at monogenetic volcanic fields. Monogenetic volcanoes *sensu stricto* are commonly assumed to erupt magma that originates from a single, compositionally homogeneous batch that ascends with limited storage in the crust. However, studies reveal that petrological and geochemical complexities exist throughout the deposits of even a single eruption, within a single volcanic edifice, and between closely spaced volcanoes within certain monogenetic volcanic fields (Johnson et al., 2008; Crummy et al., 2014; Cortés et al., 2015; Shane & Coote, 2018). Those complexities appear to be related to the development of prolonged magma storage in the crust, facilitating crustal contamination and mixing among distinct batches of melt. Observations made at exposed shallow plumbing systems, such as the San Rafael subvolcanic field (SRVF, Williams, 1983a; Delaney & Gartner, 1997), Big Bend sills in Texas (Carman, 1994), or the Otoge volcanic complex in Japan (Geshi, 2001) support these hypotheses and are supported by geophysical surveys (Cartwright & Hansen, 2006; Thomson & Schofield, 2008; Burchardt & Galland, 2016; Jerram & Bryan, 2017; Planke et al., 2017).

This study focuses on the SRVF in Utah (Fig. 1a), located in the northern transition zone between the Colorado Plateau and the Basin and Range Province. The exceptionally well

exposed plumbing system of the SRVF provides an unparalleled natural laboratory of shallow magma storage and of petrogenetic processes that occur in-situ (Delaney & Gartner, 1997; Diez et al., 2009). At SRVF, lenses and sheets (up to 3 meters thick) of coarse-grained syenite (48 to 54% SiO_2) occur totally enclosed in basalt in the upper and central portions of volumetrically large (and up to 30 m thick) sills (Gilluly, 1927; Williams, 1983a). Gilluly (1927) suggested that syenite was intruded as a separate event from basaltic intrusion, whereas Williams (1983a) and Delaney & Gartner (1997) concluded that syenite was differentiated in the sills after emplacement of the basaltic magma, and that liquid segregation was the main process responsible for the syenite being totally enclosed in "basanite". Studying the petrogenesis of SRVF magmas gives insight into processes that can occur at intraplate monogenetic volcanic fields, especially *in-situ* differentiation at shallow levels in sills that could generate appreciable quantities of evolved melts. We present in situ mineral chemistry, whole-rock major and trace element, and whole-rock Sr and Nd isotopic data on samples (n= 125) from the SRVF. The mafic igneous rocks preserved in conduits, dikes, and sills are used to constrain the magma source composition and subsequent processes that occurred during emplacement and storage of the melts. Whole rock major elements, trace elements, and radiogenic isotope data are used along with mineral data to constrain the origin of the magmas and the physical parameters such as pressure and temperature of crystal-melt equilibrium, melt viscosity and density, which can affect magma emplacement and eruptive processes at the transition between sills, feeder dikes, and conduits. Additionally, we model the chemical differentiation of the most mafic magmas to constrain parameters of crystallization that can generate evolved hydrated melts in shallow sills and therefore increase explosivity.

GEOLOGIC SETTING

The SRVF is located on the northwestern margin of the Colorado Plateau (Fig. 1a), which consists of a ~40 km-thick crust, made of 3 – 5 km thick Phanerozoic sedimentary rocks overlying a Precambrian igneous and metamorphic basement (Thompson & Zoback, 1979; Reid et al., 2012). The lithosphere-asthenosphere boundary is estimated to be at depths of 110 – 125 km (Thompson & Zoback, 1979; Reid et al., 2012) at the center of the Colorado Plateau. This depth decreases to 70 – 90 km toward the edges, where it transitions to the Basin and Range Province to the west and Rio Grande rift to the east (Thompson & Zoback, 1979; Reid et al., 2012). Flat subduction of oceanic lithosphere dominated during the Late Cretaceous through the early Cenozoic and was responsible for voluminous magmatism in the southern Rocky Mountains during this time (Tingey et al., 1991; Humphreys, 1995). Slab rollback and lithosphere delamination during the Neogene resulted in crustal extension along the margins of the Colorado Plateau. This was followed by voluminous intraplate volcanism along the transition zone between the Colorado Plateau and the Basin and Range Province (Fig. 1a), between 30 Ma and 800 yrs B.P (Smith & Luedke, 1984; Tingey et al., 1991; Gonzales & Lake, 2016).

The SRVF, between the Waterpocket monocline and the San Rafael Swell (Fig. 1b), is a deeply eroded Pliocene volcanic field in which dikes, conduits, and sills are now exposed. Primitive magmas intruded the sedimentary Jurassic San Rafael Group (Carmel, Entrada, Curtis, and Summerville Formations; Gilluly & Reeside, 1928) between 3.7 and 4.6 Ma (Delaney & Gartner, 1997). The stratigraphic position of the intrusions and the presence of vesicles in the igneous rocks suggest shallow (<1 km) depths of emplacement (Williams, 1983a; Diez et al., 2009; Richardson et al., 2015). It has been estimated that about 800 m – 1 km of overlying material has been removed by erosion since the end of volcanic activity (Richardson et al.,

2015); it is thus impossible to constrain what the volcanic field looked like at the time of eruption. Nevertheless, it is hypothesized that the SRVF was a monogenetic volcanic field based on the number of dikes (~2,000), sills (~12), and conduits (63) mapped and their spatial distribution (Diez et al., 2009; Kiyosugi et al., 2012). The sill names in the SRVF correspond to the main geographic areas (Fig. 1b): Hebes (HS), Bad Luck (BL), Cedar Mountain (CM), Frying Pan (FP), Gypsum Springs (GS), and Little Black Mountain (LBM). Solomon Temple (ST) and Moroni Buttes (MB) are relatively low areas where no sills are found, but instead are areas where dike segments and conduits protrude over the flat topography.

The intrusive features and rocks have been described in previous studies (Williams, 1983a; Delaney & Gartner, 1997; Diez et al., 2009; Kiyosugi et al., 2012; Richardson et al., 2015). Sills, more resistant to erosion, form the capping units of regional mesas (isolated flat-top hills), resulting in topographic highs throughout the field, with relief varying by about 500 m. Sills, which are mostly concordant and generally emplaced near the top of the Entrada formation (Williams, 1983a), dip shallowly (<10°) to the W or SW on the SW limbs of anticlines and NE limbs of multi-kilometer-scale synclines. Sills are roughly semi-circular, but irregular in shape, with maximum lengths of 3-5 km, and thickness typically decreasing in the down dip direction (Delaney & Gartner, 1997; Richardson et al., 2015). Additionally, some of these sills, such as those in the western Cedar Mountain and the Frying Pan areas, can be associated with specific dikes as a source for their emplacement. In each instance where this correlation is possible, most of the sills are present on the down dip side of the source dike, indicating that the magma flowed down dip during emplacement. This fact seems to indicate that the melt was above its level of neutral buoyancy at the time of emplacement (Richardson et al., 2015). Combining terrestrial and airborne laser scanning surveys, as well as detailed field mapping, the exposed plumbing system

in the north-eastern part of the SRVF was reconstructed and volumes of sills, dikes, and conduits estimated (Richardson et al., 2015). In this ~50 km^2 area, seven distinct sills were identified (Richardson et al., 2015), along with 16 conduits and 180 dikes (Kiyosugi et al., 2012). Sill thicknesses range from <5 m to >40 m, their volumes range from 10^{-4} to 10^{-1} km^3 for a cumulative volume of ~0.4 km^3. In comparison, dikes and conduits represent only 7% of the intrusive volume (0.03 km^3). Note that although Richardson et al. (2015) focused on a relatively small portion of the SRVF, they investigated the largest and thickest sills. Volume extrapolated to the entire field is still <1 km^3, making our study particularly useful to compare to monogenetic volcanic fields (Connor & Conway, 2000; Kereszturi et al., 2013).

Most dikes crosscut the sills, exhibiting weakly chilled margins. Dikes form thin, near-vertical sheets that are 0.2 to 6 m wide, with *en-echelon* segments that are generally less than 2 km in length but can reach up to 9 km in some instances (Diez et al., 2009; Kiyosugi et al., 2012). The dikes trend parallel to the western boundary of the Colorado Plateau, with a mean strike of N14°W (Delaney & Gartner, 1997). Finally, conduits are plug-like bodies assumed to have fed a volcanic edifice at the surface, based on abundant brecciation, mechanical erosion of conduit walls, and thermal erosion of xenoliths (Diez et al., 2009; Kiyosugi et al., 2012). Some plugs also appear to have been congealed in the shallow crust and hence magma did not reach the surface through those pathways (Diez et al., 2009).

Within the SRVF two types of intrusive rocks have been observed (Fig. 2): (1) a fine-to medium-grained alkalic (trachy) basalt (44 – 46 wt % SiO_2) with an aphanitic to porphyritic groundmass, and (2) a medium-to-coarse-grained leucocratic syenite (~47 – 54 wt. % SiO_2) with holocrystalline texture and frequent ophitic texture (Williams, 1983a; Delaney & Gartner, 1997). Basalt is the dominant rock type across the field and is found within dikes, sills and conduits.

Syenite is found almost exclusively inside basaltic sills, where it generally occurs in the central and upper part of the sill (Fig. 2a) and has been found also at the core of some volcanic conduits (Diez et al., 2009; Kiyosugi et al., 2012). The presence of both syenite and basalt in sills led previous authors to suggest the separation of the two melts during the late stage of crystal fractionation, most probably due to silicate-liquid immiscibility or *in-situ* crystallization, or both (Williams, 1983a; Carman, 1994). The occurrence of syenite in thin (a few cm thick) veins also suggests segregation and viscous flow of syenite through the basalt due to the action of gravitational and surface tension forces (Diez et al., 2010). Syenite is totally enveloped by basalt, and occurs as ocelli, globules (Fig. 3e), veins, lenses, and 1 to 3 m-thick sheets, while lacking chilled contacts with the basalt (Fig.2, Gilluly, 1927; Williams, 1983a). In one instance, thin sheets (~1 m thick) of syenite underlay a basaltic sill, with a flat contact but no chilled margins, implying comagmatic emplacement (Diez et al., 2010). Finally, syenite is not found in every basaltic sill, and there are no isolated sills composed exclusively of syenite. A minimum thickness of ~ 10 m is required for a basaltic sill to allow syenite to completely separate. When this condition is met, the volume of syenite completely separated into sills and interstitial veins is between 30 and 40% of the basaltic sill volume and increases beyond 50% in the thickest (>~20m) sills. According to our mapping, no syenite is found in the sills of Gypsum Springs, Solomon Temple, or Moroni Butte but a core of syenite is present in the only mapped conduit in the Gypsum Springs area (Wetmore, unpublished mapping).

MATERIAL AND METHODS

Sampling

A hundred and twenty-five samples were collected from dikes, sills, and conduits interiors at various locations throughout the entire SRVF, as well as country rocks, namely the Entrada and Curtis formations, avoiding loose boulders and weathered surfaces (Fig. 1c). A list of sample names, rock types and locations can be found in supplementary material EA1. Note that all syenite samples analyzed have been collected from syenite sheets (1 – 3 m thick) found within basaltic sills. Location names refer to the topographic highs corresponding to main sill bodies (Fig. 1b): Hebes (HS), Bad Luck (BL), Cedar Mountain (CM), Moroni Buttes (MB), Frying Pan (FP), Gypsum Springs (GS), Solomon Temple (ST), and Little Black Mountain (LBM).

Major and trace element analyses

Samples were analyzed for whole-rock major and trace elements at the Center for Geochemical Analyses at the University of South Florida. Whole-rock samples were wrapped in plastic, chipped using a sledgehammer, weathered parts were removed, and fresh interior were powdered in a high-alumina shatterbox for 15 minutes. Approximately 2 g of each powdered sample was weighed in high-alumina crucibles and heated in a furnace at 200°C for 15 minutes, cooled and weighed again, and then heated at 1025°C for another 15 minutes and weighed again to measure the loss on ignition (LOI). For major element analyses, flux fusion (modified after Murray et al., 2000) was conducted on 0.1 grams of sample mixed with 0.4 grams of flux ($LiBO_2$) in a graphite crucible. Blanks were prepared with 0.4 grams of flux only. Samples were heated to 1075°C for 15 minutes until completely melted and then poured into a polypropylene container filled with 50mL of 2M HNO_3 and 10 ppm Ge internal standard solution and mixed until dissolved to create a 500x dilution. The solutions were then diluted to 10,000x by taking 2.5mL of the made solution and mixing it with another 47.5 mL of 2M HNO_3 plus 10ppm Ge solution. Calibration

standards BCR-2, STM-1, JA-2, JP-1, JR-1, W-2, JB-3, BIR-1, and BHVO-2 (values from GeoReM, Jochum et al., 2005), as well as internal standard JB-3 (EA2) were prepared similarly to the unknown samples. Solutions were analyzed using a Perkin Elmer 2000 DV Inductively Coupled Plasma Optical Emission Spectrometer (ICP-OES) with an analytical precision better than 5%. Sample preparation for trace element analyses was conducted using HF-HNO_3 acid digestion after Kelley et al (2003) and measured using a Perkin Elmer Elan DRC II Q-ICP-MS (ICP-MS). Calibration standards for trace element analysis include USGS-BHVO-2, BIR-1, BCR-2, W2, SY-2, and JP-1; GSJ JA-2, JA-1 and NBS SRM 688. Standard deviation and error were measured on SRM GSJ-JB-3 and generally better than 3% for most elements on the ICP-MS (Table EA 2). Table EA2 contains quality control data for ICP-OES and ICP-MS analyses. Whole-rock major element and trace element data are reported in supplementary material EA3 and EA4, respectively. Using whole-rock major element data, we have recalculated Fe_2O_3 and FeO using a ratio of 0.16 as advised by Cottrell and Kelley (2011). We have also calculated Mg# using equation 1 below:

$$Mg\# = MgO/((FeO+MgO))\times 100 \qquad [Eq.\ 1]$$

$^{87}Sr/^{86}Sr$ and $^{143}Nd/^{144}Nd$ isotopic analyses

A total of 15 igneous samples, plus two from the country rocks (one Entrada sandstone and one carbonate from the Carmel formation) were analyzed to determine their $^{87}Sr/^{86}Sr$ and $^{143}Nd/^{144}Nd$ isotopic ratio (Table 1). Strontium (Sr) and Neodymium (Nd) isotope ratios were measured on aliquots from the same unspiked rock powders that were used for the major and trace element analyses. The samples were dissolved in ultrapure HNO_3:HF acid mixture (1:3), followed by dry

down and re-dissolving in optima grade ultrapure HNO_3 acid and subsequent dry down and digestion in ultraclean HCl acid. The final clear solutions were centrifuged and treated by conventional ion-exchange chromatography (using AG50WX-8 resin for Sr and AG1X-8 and LN Spec resins for the REE fraction) in the clean lab of University of Leeds. Following Sr and Nd purification, samples were loaded onto previously outgassed W (for Sr) and Re (for Nd) pure metal filaments. Sr and Nd isotope ratios were measured on a Thermo-Fisher *Triton* series multi-collector thermal ionization mass spectrometer running in static mode. The normalization ratio used for Sr fractionation correction was $^{86}Sr/^{88}Sr = 0.1194$ and for the Nd it was $^{146}Nd/^{144}Nd = 0.7219$. Instrument errors for determinations of $^{87}Sr/^{86}Sr$ of $^{143}Nd/^{144}Nd$ ratios are reported as 2σ. External precision (2σ) for Sr and Nd isotopic ratios from successive replicate measurements of standards (NBS 987, BHVO-1 USGS, and La Jolla) was better than 15 ppm. The NBS-987 normalized (to 0.710248) $^{87}Sr/^{86}Sr$ ratios of BHVO-2 standard gave values of 0.703506, whereas those of La Jolla- normalized (to 0.511858) $^{143}Nd/^{144}Nd$ ratios were 0.512928, i.e. in agreement with the values for the same standards reported in the literature (Weis et al., 2006; $^{87}Sr/^{86}Sr= 0.703475$ and $^{143}Nd/^{144}Nd= 0.512986$). Analytical results are presented in Table 1. The Sr and Nd concentrations were measured via ICP-MS together with the other trace elements (Table EA4). The total chemistry blanks for Sr and Nd were negligible during the period of measurements (0.4 ng for Sr and 0.3ng for Nd).

Electron microprobe analysis

Thin sections of 31 samples were prepared for petrographic examination and major element mineral analysis on an electron probe micro analyzer (EPMA). For twenty-seven samples, chemical analyses were conducted at the Florida Center for Analytical Electron Microscopy

(FCAEM) at Florida International University, Miami, FL, on a JEOL 8900R Superprobe EPMA. For five samples, in-situ major element mineral chemistry was analyzed at the University of Leeds Electron Microscopy and Spectroscopy Center (LEMAS) using JEOL JXA 8230 electron microprobe. On both instruments, minerals were analyzed at 15kV accelerating potential and 10 – 30 nA beam current using a 2µm-wide point beam. All elements were measured for 10 seconds on peak and data were corrected using a ZAF (atomic number, absorption, fluorescence) correction procedure. Calibration was completed on known minerals prior to analysis. All Fe collections are reported as FeO. For the analyses processed at FCAEM facility, the following internal standards were used for primary calibration for each element. Si : Olivine, Plag An65, Augite, Muscovite, and Alm-Garnet; Al : Muscovite, Augite, BHVO2, and Plag An65; Na : Plag AN65; MgO : Alm Garnet, Augite, Olivine, and Biotite; K: Sanidine and Muscovite; Ca : Alm Garnet, Augite, Plag An65, and Diopside; Fe : Olivine, Muscovite, and Alm Garnet. For primary instrument calibration at LEMAS facility, the standards used were as follows: Si : GEO2 diopside or olivine; Ca : GEO2 diopside; Mg : GEO2 diopside or olivine; Fe : GEO2 hematite; Ti : GEO2 Rutile; Cr: GEO2 Cr_2O_3; Mn : GEO2 Rhodonite; Na : OB4 Jadeite; K : GEO2 Kspar; and Al : GEO2 Kyanite. The same minerals were used as secondary standards and their measured values compared to the accepted values of standard GEO2. The olivine on the GEO2 mineral standard block has Mg/Fe zonation, resulting in high standard deviation in the olivine standard and unknown data (Pankhurst et al. 2016). Accepted and measured values of standards for each facility are presented in the electronic table EA2. Several crystals of pyroxene, plagioclase, oxide, olivine, amphibole, and biotite were analyzed for each available thin section. Within each crystal, multiple points were analyzed to account for possible differences between core and rim.

Details about which analytical facility was used are given along with microprobe results in the supplementary material tables EA5 to EA8.

RESULTS

Petrography and mineral compositions

About half of the samples collected showed no visible signs of alteration, and therefore are considered fresh based on their appearance in the field and in thin section, with no vesicles, no secondary remineralization, and primary olivine that has not been serpentinized (Table EA1, Fig. 3). Samples with moderate weathering (~ 40% of all samples) have a thin oxidized weathering rind, with surface vesicles filled by secondary mineralization such as zeolite, but fresh interiors. Moderately weathered samples have partially serpentinized olivine (Fig. 3g and 3h), but no sign of further alteration of their groundmass. Eleven samples are highly weathered as their olivine crystals are serpentinized (Fig. 3i and 3j), with secondary clay mineralization on the rock's surface, and overall discoloration of their interiors, confirmed by petrography and the more elevated loss on ignition values (EA1). For all samples, chemical analyses were processed on powders obtained from unaltered samples and from the fresh interiors. Mineral modes are averaged by rock type in Table 2, and details for each sample studied in thin section can be found in supplemental table EA1.

Alkalic basalts of the SRVF are melanocratic and porphyritic, with up to 60 vol. % crystals scattered in an aphanitic to microcrystalline groundmass (Fig. 2d, 3a, and 3b). Phenocrysts, generally between 0.5 and 2 mm, are olivine (15 - 55%), clinopyroxene (5 – 60%), feldspars (15 – 25%), and oxides (5 –15%), with some samples containing phenocrysts of biotite

and/or amphibole (5 – 15%). Phenocrysts are enclosed in a groundmass of olivine, pyroxene, and plagioclase (Fig. 3a). Feldspar phenocrysts are commonly plagioclase, with some rare sanidine. In about 50% of the samples, olivine crystals are fresh, rare crystals are partially serpentinized along fractures (Fig. 3g and 3h), and 11 samples have complete serpentinization of olivine (Table EA1, Fig. 3i and 3j). When present in basalt, biotite crystals range in size from 0.2 mm to 1 mm, and amphibole crystals are < 0.5 mm in size.

SRVF syenites are unaltered leucocratic holocrystalline rocks with phaneritic textures (Fig. 3b). Crystals range in size from 0.5 mm to 2 cm, with some that may reach up to a few cm (Fig. 2). Feldspar is the dominant mineral phase (35 – 50 vol.%) with equal amounts of plagioclase and sanidine. Biotite and amphibole (10 – 25%) form large crystals often up to a few centimeters in length (Fig. 2 and 3). Clinopyroxene (10 – 30 %) and Fe-Ti oxide (10%) are also present, along with rare olivine, partially serpentinized, in a few samples.

Feldspars in both rock types, up to 5 mm in size in syenite, are subhedral to anhedral, generally not zoned, and with only rare twinning. Anorthite (An) contents in plagioclase range between An_{64} and An_{77} (Fig. 4a and EA5), except for two samples from Little Black Mountain sill (LBM-01 and LBM-10) in which plagioclase crystals have lower sodium contents, with compositions of ~An_{40}. Orthoclase content in sanidine is Or_{50-65}.

Clinopyroxene phenocrysts in both the syenites and basalts are generally subhedral to anhedral, not twinned, and without exsolution textures. Crystals range in size between 0.5 and 2 mm. In some basalts, some grains have a sieved core (Fig. 3k and 3l), probably generated during ascent after being remobilized from a deeper storage region. Often, we checked for possible zonation by analyzing the core and the rim of the same grains (EA6). Compositions measured by electron microprobe (EA6) appear to be homogeneous regardless of the type of rock (syenite or

basalt) and plot as diopside ($En_{32}Wo_{42}Fs_{26}$ – $En_{34}Wo_{52}Fs_{14}$, Fig.7b) with 2 – 10% Al_2O_3, 10 – 18% MgO, and Mg# of 0.65 – 0.85 (EA6). One syenite sample, BL-05, has pyroxene with lower Mg# (0.50 – 0.67) and higher FeO (11 – 17%), with a composition of $En_{33}Wo_{43}Fs_{24}$.

Amphibole phenocrysts are generally large (0.2 – 5 cm), with euhedral shapes and are found almost exclusively in the syenites. Amphibole classifies as pargasite with the following chemical composition: Mg# of 0.64 – 0.78, FeO_t from 9.71 to 13.51%, and CaO from 10.79 to 13.46% (EA7).

Biotite occurs as medium-size crystals (0.1 – 1 cm) in the syenites (25 vol.% of all phenocrysts) and are present as intergrowths with pyroxene and amphibole. Molar Mg# ranges from 0.58 to 0.90, with most values clustered around 0.66, and K_2O varies from 4.44 to 10.35%, independent of rock type (EA7). Crystals are generally unaltered in both rock types, and textural relations with adjacent minerals suggest late crystallization.

Titaniferous magnetite with between 8.7 and 10.3 wt. % TiO_2, occur as relatively small euhedral grains in both the basalts and the syenites (EA7). Ti-Magnetite may occur as individual grains or in association with biotite, olivine, or pyroxene.

Whole-rock geochemistry

Loss on Ignition (LOI) values (EA3) range from 1.6 to 9.4 wt.% for basalts (with 70% of basalts having LOI in the range 3.6 – 7.5 wt.%), and from 1.5 to 6 wt.% for syenites (with 45% of syenites having LOI in the range 4.6 – 5.6 wt.%). Given the lack of secondary mineralization in the samples analyzed, the higher LOI values likely reflect the serpentinization of olivine in basalts, as well as the presence of biotite and amphibole in syenites.

The SRVF whole rock compositions are shown on a Total Alkalis vs Silica (TAS) diagram (Figure 5), where they range from gabbro to foid-monzosyenite, with the majority falling within the monzogabbroic field. Extrusive equivalents range from alkali basalts to phonotephrites. Basalts tend to be slightly more mafic (Mg# 41 – 65 with median value at 58; Supplemental Table EA2) when compared with the associated syenites (Mg# 26 – 58 with median value at 39). Additionally, compared to the basalts the syenites have much higher alkali content (see red symbols in Fig. 5). Using Lange et al. (2009) plagioclase hygrometer, we have calculated dissolved water concentrations (wt% H_2O) for samples from which plagioclase compositions have been analyzed by EPMA. Basalts have 0.1 to 1 wt.% H_2O and syenites 3.4 to 3.7 wt.% H_2O (Supplementary Table EA3). A CIPW norm calculation including biotite and hornblende (Hutchison, 1974) was processed using GCDKit software (Janoušek et al., 2006), and detailed results are presented in EA3. Independent of their composition, SRVF basalts and syenites have about 40 norm.% Plagioclase (Pl), 20 norm.% Biotite (Bt), 5 norm.% Wollastonite (Wo), 2.5 norm.% Magnetite (Mt), 2.5 norm.% Illmenite (Il), and 2 norm.% Apatite (Ap). None of the syenite samples have normative quartz (Qz), and only 39 basalts have 0.3 to 7% normative Qz. All syenites have 5 to 18% normative Orthoclase (Or). Normative Or (< 3%) was calculated only for five basalts from Cedar Mountain and Bad Luck sills. All syenites and 15 basalts have normative nepheline (Ne) between 1 and 20 norm.%. Almost all basalts (95%) have a normative mineralogy that does not include olivine but includes 20 norm.% hornblende, although no amphibole is present in our natural samples (Table 2, and EA1).

On a tectonic discrimination diagram, trace element compositions show no variations for various geographic areas throughout the field (Fig. 6), with higher Ta and Th concentrations than the average regional upper crust (UC), Sub-Continental Lithospheric Mantle (SCLM) or Oceanic

Island Basalts (OIB). Chondrite-normalized rare-earth element (REE) patterns display an enrichment in light REE (LREE) relative to the heavy REE (HREE) similar to intraplate basalts (Fig. 7a), with flat HREE patterns indicative of relatively shallow mantle source above the garnet stability field (< 85 km depth). Primitive mantle normalized data display patterns (Fig. 7b) characteristic of intraplate basalts, but also with classic LREE and LILE enrichment and slightly negative spikes for the HFSE such as Nb, Zr, Ti, probably due to the involvement of a metasomatized mantle source.

$^{87}Sr/^{86}Sr$ and $^{143}Nd/^{144}Nd$ isotopic ratios were analyzed in basalts from five conduits, four dikes and four sills, and also in syenites from two sheets enclosed in basaltic sills (Table 1). One sample of the Entrada sandstone and one carbonate from the Carmel formation collected at a contact with one plug were also analyzed. Results are presented in Table 1 and plotted on Fig. 8. All igneous samples have a restricted range in $^{87}Sr/^{86}Sr$ (0.7045 – 0.7051) and $^{143}Nd/^{144}Nd$ (0.51224 – 0.51241) supporting co-genetic origin of the SRVF melts. The two Jurassic sandstone and carbonate samples, representing the local country rocks, both with elevated $^{87}Sr/^{86}Sr$ values, with ratios of 0.7088 and 0.7119, respectively. The host rock (sample TT-11) at the contact with a conduit has similar $^{143}Nd/^{144}Nd$ (0.51230) to the igneous samples, whereas the Entrada sandstone has a lower (more radiogenic) Nd isotope ratio of 0.51220 (Fig. 8).

Mineral-melt thermobarometry

To constrain the magmatic pressures (P) and temperatures (T), we apply mineral-melt equilibria geobarometers and geothermometers designed by Putirka (2008). We use pairing of clinopyroxene and whole-rock compositions (representing the initial crystal-free melts). Based

on the observed mineralogy and calculation of dissolved water using Lange et al. (2009) hygrometer, we use 1 wt.% H_2O in basalts, and 3% of H_2O in syenites, and consider results given for hydrous systems (equation 33 in Putirka et al., 1996). The 233 clinopyroxene crystals analyzed have Mg# ranging from 50 to 88 (EA6), most of the crystals (n=185) having Mg# 70 – 80, the lowest values being encountered in pyroxenes from syenites (Mg#: 50 – 75). Calculated Fe-Mg partition coefficients $K_D(Fe\text{-}Mg)^{CPX\text{-}LIQ}$ between clinopyroxene (CPx) and host melt range from 0.11 to 1.26 (EA6). Additionally, the sum of clinopyroxene components approaches unity, and the calculated components are similar to analyzed compositions, suggesting that crystals are at equilibrium with the host melt (Putirka, 2005). For basalts, CPx crystallizes from magma with T= 1245 to 1081 ± 66 °C and P= 14.3 to 1.9 ± 0.4 kbar. Using a density of 2.7 g/cc for the crust (Thompson & Zoback, 1979), this corresponds to depths between 54.2 and 7.2 km (Fig. 9), with most of the crystals forming at depths between 30 and 22 km. In syenite, CPx crystallizes at T= 1016 to 992 ± 30°C and P= 0.98 to -0.53 (effectively 1 atm) ± 0.11 kbar, corresponding to depths shallower than 2 km (Fig. 9).

DISCUSSION

Origin of the parental melts

Whole-rock major and trace element, and radiogenic isotope compositions for SRVF igneous rocks reveal a common magmatic origin. SRVF samples spread across the fields of intraplate zones and active continental margins (Fig. 6), consistent with the regional geologic setting where magmatism results from extension at the edges of the Plateau with upwelling of a metasomatized mantle. All samples display overlapping REE abundances, with enriched LREE and flat HREE

patterns (Fig. 7a), suggesting melt generation in the mantle above the garnet stability field, i.e., <85 km (Robinson & Wood, 1998). The Primitive Mantle (PM)-normalized multi-element patterns for the SRVF samples (Fig. 7b) might reflect the nature of the metasomatized sub-continental lithospheric sources. Chondrite-normalized REE plot for SRVF samples is typical of intraplate alkali basalts. This intraplate component is consistent with slab steepening and lithosphere delamination occurring after 26 Ma, generating an asthenospheric influx (Alibert et al., 1986; Tingey et al., 1991; Gonzales & Lake, 2016).

The restricted range in $^{87}Sr/^{86}Sr$ and $^{143}Nd/^{144}Nd$ isotopic ratios in SRVF basalts and syenites reveal that the SRVF magma source has isotopic characteristics similar to the EM-I reservoir proposed for some OIB suites (Hofmann, 1997), plotting just below the mantle array (Fig. 8). Importantly, the SRVF rocks plot within the field defined by other volcanic suites from Utah's transition zone between the Colorado Plateau and the Basin and Range Province (Kempton et al., 1991). In contrast to volcanic fields from the southern transition zone (central Arizona to New Mexico), the SRVF lacks evidence for crustal assimilation as it maintains lower $^{87}Sr/^{86}Sr$ in comparison with the local host rocks (Entrada Sandstone and Carmel limestone Formation) and regional crustal compositions (Fig. 8c). The influence of an EM-I type mantle affecting mostly the Utah transition zone volcanic fields (Fig. 8c) might reflect the signature of a SCLM metasomatized by slab-impacted melts during ancient subduction (Gonzales & Lake, 2016). Additionally, ratios of high field strength elements (HFSE) to LREE in the SRVF samples, (e.g. Nb/La) that range from 0.26 to 0.93 (Fig. 5b and EA2) are indicative of a significant influence of the lithospheric mantle (Fitton et al., 1991; Faust, 2005) and more closely resemble melts generated from mantle beneath the Colorado Plateau than those from Basin and Range Province (Kempton et al., 1991).

To evaluate the petrogenetic processes in relation to the tectonic setting, we have used the most primitive (highest mg# and lowest alkalis) whole-rock chemical compositions of basalts (samples GSC-04, GSC-06, LBM01, LBM06, FP-03, and FP-07) as proxies for primitive melts. We estimated mantle potential temperatures in the range of 1260 – 1326°C using the method of Lee et al. (2009) and accounting for 1% H_2O. This method was calibrated for dry mafic magma, and since the SRVF basaltic samples are expected to have at least 1 % water with melts originating from a metasomatized mantle, we expect the temperatures of the SRVF source to be slightly lower than those calculated. Additionally, pressures of partial melting calculated with the same method range between 1.2 and 1.9 GPa, which correspond to depths of 70 – 48 km. These temperatures and pressures allow us to define a melting column that is at the base of the subcontinental lithospheric mantle, consistent with the melting depths suggested for other Colorado Plateau volcanic fields (Wang et al., 2002; Faust, 2005; Reid et al., 2012). Considering that pyroxene in basalts crystallize as deep as 50 km, this reduces the melting column to 70 – 50 km deep.

The large trace element dataset available and its spatial distribution are ideal to create large-scale geochemical maps (Fig. 10) using an Inverse Distance Weighting Interpolation from ArcMap 10®. Only basalts are used for the interpolation as they represent the most primitive SRVF compositions. The Ba/Ta (LILE/HFSE) ratios that would represent the influence of a metasomatized SCLM vary from 884 to 3049. However, the map shows that most of the field has a relatively restricted range that only varies 2-fold. Nb/Ta ratios, both highly incompatible elements, do not show significant variations (11.7 – 18.6), and are representative of a rather homogeneous source at this scale across the field. Such low ratios are also likely to reflect the metasomatized SCLM. In both cases, extremely high values located at the edges of the field and

isolated conduits likely are artifacts from the interpolation due to the lack of data outside of the field.

Whole-rock major and trace element, and radiogenic isotopic compositions are consistent with the interpretation that two source components participate in melt generation beneath the SRVF: (1) an enriched asthenospheric mantle source, and (2) a metasomatized lithospheric mantle corresponding to the SCLM. These observations are consistent with geochemical signatures observed at other Pliocene volcanic fields in the transition zone between the Colorado Plateau and the Basin and Range Province (Tingey et al., 1991; Cortés et al., 2015; Gonzales & Lake, 2016). Within those fields, Pliocene mafic lavas have asthenospheric geochemical signatures of intraplate alkali basalts that are related to upwelling of a depleted mantle source due to slab rollback and lithospheric delamination during the Miocene (Gonzales & Lake, 2016), associated with a signature inherited from metasomatism of the SCLM (Crow et al., 2011; Ballmer et al., 2015).

In-situ differentiation of basalt

Crystallization conditions

The clinopyroxene-liquid thermobarometer reveals that basalts crystallized between 13.4 – 1.4 kbar and 1223 – 1076°C, whereas syenites crystallized between 1.2 and -0.3 kbar and at about 1000°C (Fig. 9). This corresponds to crystallization depths of 50 to 5 km for basalts and < 4 km for syenites (Fig. 9). Moreover, syenite clinopyroxenes define a nearly isobaric set of crystallization conditions, whereas basalt clinopyroxenes define a broader range of temperatures and depths of crystallization. These results indicate that primitive mafic melts crystallized during

ascent from at least 50 km deep with limited storage in the Colorado Plateau lithosphere. Such depths are consistent with the model in depth of crust, lithospheric mantle, and asthenosphere based upon seismic refraction data (Thompson & Zoback, 1979; Condie & Selverstone, 1999). Our results indicate that basalt crystallized while ascending through the Precambrian igneous and metamorphic basement. Syenite began crystallizing when the basalt, in the form of a crystal mush, intruded Phanerozoic sedimentary rocks, more specifically the Jurassic San Rafael Group, whose depth was estimated to be ~ 1 km below the surface at the time of magmatism (Richardson et al., 2015), roughly 4 Ma ago. These results are consistent with previous studies at SRVF (Williams, 1983a; Delaney & Gartner, 1997), suggesting that basaltic magmas ascended from the asthenosphere with minimal time spent in storage in the crust, and thus with no evidences of crustal assimilation, as revealed by isotopic compositions (Fig. 8).

Petrogenetic modeling

Whole-rock and mineral chemistry suggest that SRVF basalts and syenites are comagmatic. More specifically, syenite samples tend to be more evolved than the basalts (Fig. 5 and EA3), and geochemical data suggest an evolution from mafic magmas with SRVF composition. To constrain the parameters controlling the evolution of the SRVF magmas (from basalt to syenite), we used the COMAGMAT-3 magma crystallization model. COMAGMAT-3 (Ariskin, 1999) is a thermodynamic program developed to compute crystallization of silicic melts. To model the evolution of the SRVF magmas, an initial liquid composition is chosen, and the temperature is decreased at regular intervals defined by a specific increment of crystallization (in wt. %). Studies on various shallow intrusions in different tectonic settings suggested that sills solidify via equilibrium crystallization (EC, Marsh, 2002), while others inferred that sills solidify quickly

enough to prevent crystals from interacting with the interstitial melt, suggesting an evolution by fractional crystallization (FC) instead (Zavala et al., 2011). We choose to run the COMAGMAT-3 models for both EC and FC conditions to test for both hypotheses. We adopted results from thermobarometry as input for the possible P-T conditions applied to the system and under which magma could have evolved. The results provide estimates of the relative proportions and compositions of the fractionated minerals and evolution of the residual liquid composition, defined as the liquid line of descent (LLD) that can be compared to the compositions observed in natural SRVF samples (Fig. 11).

We have limited our modeling to the most primitive sample (CM-10) in our dataset as a proxy for the parental magma. This sample has 45.5 wt. % SiO_2, 12 wt. % MgO, 10wt. % FeO_t, and has been sampled from Cedar Mountain sill, the largest sill complex in the SRVF (Richardson et al., 2015). The primitive liquid composition was used with the following parameters: (1) EC or FC crystallization, (2) decompression crystallization from 10 to 0.5 kbar, (3) open system with a QFM+1 oxygen buffer, and (4) H_2O content of 1 or 3 wt. %. Lange et al. (2009) hygrometer indicates the SRVF basalts may contain ~1 wt.% water, consistent with basalts in other volcanic fields along the Colorado Plateau edges, such as the San Francisco Volcanic Field (Rudzitis et al., 2016). Modeling basalt differentiation with an initial water content set at 1 - 3 wt.% is appropriate to test if dissolved H_2O concentration can increase as an incompatible constituent during fractionation and reach >3.5 wt.% in syenites. The EC and FC models give similar differentiation trends (Fig. 11), although modeling with 1 wt.% dissolved H_2O in the primitive basalt tends to match natural compositions better. In terms of water content, modeling with 3 wt.% H_2O results in appropriate water content in the evolved compositions. When looking at the crystallization sequence (Fig. 11, supplemental EA9), the FC modeling

gives abnormal results, as less than 2% of augite crystallizes, and no plagioclase, olivine, nor oxides crystallize. Finally, modeling FC with 1% water crystallizes less than 6% of the starting melt. Therefore, EC seems to be the preferred process to form syenite from basaltic crystal mush in the SRVF sills. Calculated compositions of the residual liquid match the composition of natural syenite when the original magma has crystallized 30 - 50%. Additionally, at this crystallinity, the fractionated mineral assemblage is 3-5% olivine (Fo_{89-91}), 5% plagioclase (An_{71-75}), 3-35% augite ($En_{51}Fs_7Wo_{42}$), and 5-8% magnetite ($aUlv_{5-22}$), which is consistent with the phenocryst assemblage in natural SRVF samples (Tables 2 and EA1). Unfortunately, the program does not model other mineral phases for full comparison with the natural samples. The model can produce up to 4.5 % water in the most evolved samples, which is consistent with the observed mineralogy, as syenites contain significant amounts of amphibole and biotite, and dissolved H_2O calculated from major element compositions (Lange et al., 2009).

Hydrous phases form the largest phenocrysts in syenite, where they can reach up to 5 cm in some instances (Fig. 3b). The growth textures frequently observed for amphibole and biotite crystals in the syenites might have been enhanced by the presence of water in the interstitial melt during crystallization of basalt's phenocryst assemblage of olivine, plagioclase, pyroxene, and Fe-Ti oxides. This crystallization may act as a buffer and prevent water saturation of the melts, as suggested by Beard et al. (2004). According to our mass-balance modeling, mineralogy, and the observed textures, particularly the presence of large hydrous minerals in the syenite, this reaction may have occurred as equilibrium crystallization of interstitial melt in a closed system already rich in crystals (>40% vol.) at relatively high temperatures (>900°C), similar to what has been suggested for the Smartville Pluton Complex in California (Beard & Scott, 2018) or for the Little Three dike complex also in California (Morgan & London, 1999). Coarse-grained and

pegmatitic textures have also been described in evolved sheets that differentiated within thick basaltic lava flows (Philpotts et al., 1996; Caroff et al., 1997). Our petrographic observations, supported by COMAGMAT modeling (Fig. 11), suggest that in SRVF rocks, olivine, magnetite, and pyroxene crystallize first, followed by feldspars, then biotite and amphibole, particularly in syenite where growth of the latter minerals might be enhanced by a slightly higher water content, resulting in large crystals. Development of coarser grained rocks differentiated from H_2O-rich basalt has been documented elsewhere (Caroff et al., 1997; Beard et al., 2004). Geochemical data show that syenite in the SRVF is enriched in silica compared to basalt and contains more large crystals of amphibole and biotite when compared with the basalt (Table 2). Both are hydrous minerals, supporting the evidence of enrichment of the residual melt in incompatible elements. Crystallization of large hydrous minerals may have been enhanced by water enrichment in the interstitial liquid along the solidification front - crystal network with lower crystallinity - advancing inward from the margins of the sills to the center (Fig. 12).

Melt segregation

It is possible that differentiation of melts at SRVF is a non-unique process, with a combination of equilibrium crystallization and melt segregation, allowing continued separation of a phonotephritic residual melt from a crystal mush during crystallization. Density contrast between the basaltic crystal mush and the phonotephritic interstitial liquid at similar viscosities might favor such process of melt segregation. Density and viscosity of basalt and syenite have been calculated using DensityX (Iacovino & Till, 2019) and grdViscosity (Giordano et al., 2008) programs at pressures and temperatures defined by thermobarometry calculations and mass balance modeling, i.e., from 1300°C to 1000°C and at 10 and 0.2 kbar for basalts. As mass

balance modeling suggests that syenites formed close to the solidus temperature of basalts, supported by petrography of natural samples, we have calculated density and viscosity of syenite only at 1000°C and 0.2 kbar, i.e. at storage conditions in shallow sills. Detailed density and viscosity data can be found in EA10. Basalt density averages 2.71 ± 0.05 g/cm^3 at 10 kbar and 1300°C, and 2.61 ± 0.05 g/cm^3 at 0.2 kbar and 1000°C. Syenite density averages 2.42 ± 0.05 g/cm^3 at 0.2 kbar and 1000 °C. Basalt viscosity is 2.23 Pa s on average at 1300°C, and 166 Pa s at 1000°C, and syenite viscosity at 1000°C is 142 Pa s. Close to the minimum temperature, basalt and syenite have density contrasts of ~ 0.2 g/cm^3, which could explain field observations of syenite globules within basalt and the lack of chilled margins between basalt and syenite (Fig. 2). Our petrographic observations and the calculated physical properties suggest that syenite can be physically separated from basalt by crystal mush compaction mechanism (Fig. 12). This process might have happened close to the solidus temperature of basalts and would be similar to the process of silicic segregation resulting from bimodal differentiation at the solidification front (Marsh, 2002). Within sills, crystallization occurs in a solidification zone (Fig. 12), whose front moves progressively toward the interior of the magma body away from the sill margins and can extract interstitial liquid by compaction of the crystal mush once crystallization of the system has reached ~65 % (Langmuir, 1989; Carman, 1994; Morgan & London, 1999; Geshi, 2001; Marsh, 2002; Zavala et al., 2011; Berger et al., 2017). Crystal settling and sagging in the solidification front can rupture the rigid framework and generate gravitational instabilities and segregation of liquid and crystals (Carman, 1994; Geshi, 2001; Seropian et al., 2018). In such cases, the extraction of the melt results in compositional variations that are similar to evolution by FC processes (Marsh, 2002). This process is typical of *in-situ* crystallization, frequently observed in closed systems such as layered intrusions and basaltic sills (e.g., Big Bend sills in Texas,

Carman, 1994, Ferrar dolerite in Antartica, Zavala et al., 2011), where SiO_2 content increases from the margin to the center of the intrusion (London & Morgan, 2012; Beard & Scott, 2018). Similar in-situ segregation of intermediate to evolved melts as pods and sheets have been studied within basaltic lava flows (Goff, 1996; Philpotts et al., 1996; Caroff et al., 1997; Hartley & Thordarson, 2009) and lava lakes (Helz, 1980). For large basaltic sills where this phenomenon has been investigated, segregated melts are generally 5 – 10% richer in silica than their basaltic host after 50 – 70 % crystallization (Marsh, 2002, and references therein). In those examples, contacts between the host basalt and the enclosed silicic melt generally exhibit coarser crystals, and grain size decreases toward the center of the segregated evolved body. Such textures are observed at SRVF at the contact between syenite and basalt (Fig. 2). In addition, it has been suggested that surface tension forces, which can exceed the gravitational forces, will drive melt flow toward high porosity regions, favoring formation of meter-scale lenses and sheets of syenite (Diez et al., 2010).

Sills in the SRVF are internally layered (Fig. 2), with syenite always enclosed within basalt, but they lack the rhythmic or cryptic layering characteristic of layered intrusions, such as observed in the Cenozoic Skaergaard intrusion (Holness et al., 2017). The contacts between the syenite and basalt lack chilled margins, suggesting limited thermal gradient between the two melts. This texture is consistent with *in-situ* segregation of crystals and residual liquid in a host intrusion (Geshi, 2001; Zavala et al., 2011; London & Morgan, 2012). At SRVF, syenite sheets of meter-scale thickness are found in the upper half of basalt sills that have an overall thickness often exceeding 15 m. The thickness increases up dip (Fig. 12) and in map view these variations appear to correspond to teardrop shaped diapirs of syenite that taper down-dip. The syenite melt collection in numerous silllets, dikelets, and sheets (which are, by definition, devoid of any

basalt, Fig. 2), demonstrates the fluidity of the segregated melt within the sill between the time of its emplacement and the final solidification. Sillets and dikelets are small-scale (a few cm) horizontal and vertical features concordant with the main sills and dikes. The conclusion that the parental melts flowed down the dip of the bedding planes (Richardson et al., 2015) suggests that the basaltic melts were above their level of neutral buoyancy during emplacement. By contrast, flat-bottomed, teardrop shape syenite sheets, with their thickest parts being at the highest structural levels (Fig. 12), suggest that these secondary melts were potentially below their level of neutral buoyancy and flowed back up dip following collection of a sufficient volume. Such observations are consistent with recent models of crystal-rich mushes in which melt pockets can be isolated within the crystal network, and can be remobilized to coalesce into Rayleigh-Taylor instabilities that have then the ability to focus and develop conduits that may feed eruptions at the surface (Cashman et al., 2017; Jackson et al., 2018). Such a mechanism has also been also invoked to explain the presence of cylinders and diapirs of evolved melts engulfed within basalts in thick lava flows, lava lakes, sills, and laccoliths (Helz, 1980; Goff, 1996; Puffer and Horter, 1993; Caroff et al., 1997).

Conceptual model of the intrusions in the SRVF: Implication for melt evolution and segregation in basaltic shallow plumbing systems

The exposed plumbing system of the SRVF provides a comprehensive picture of shallow magma storage and of *in-situ* petrogenetic processes. We suggest that the SRVF intrusive features were sourced from magma batches that originated above the garnet stability field in the asthenospheric mantle and ponded below the crust-mantle boundary (Fig. 12). Magma ascended through dikes in the brittle upper crust, have stalled in shallow sills, and eventually formed conduits that fed

eruptions (Fig. 12). Basalt magmas started to crystallize during ascent up to about 5 km below the surface. The level of neutral buoyancy is attained about 1 km below the surface and magma - now close to a crystal mush system - intrudes laterally, developing sills (Fig. 12b). Fractionation in the sills occurred via *in-situ* crystallization, during which solidification fronts propagate inward from sill boundaries until they eventually meet toward the center of the sill (Fig. 12 c). At those fronts, residual liquid enriched in incompatible elements, including water, accumulates and forms a network of evolved melt and crystals in pods, lenses, and sheets. Syenite, being less dense but still relatively fluid, separates from the basalt host. Crystallization of amphibole and biotite is enhanced in the syenite by reaction of the interstitial melt with the mafic minerals (mostly pyroxene and Fe-Ti oxide), generating a coarse-grained texture in the syenite with grain size gradually decreasing away from the syenite-basalt contact (Fig. 12c).

It has long been assumed that small-volume basaltic volcanoes, particularly cinder cones, undergo limited differentiation. However, a few studies of long-lived (> 1 yr) basaltic eruptions show that magmatic evolution over the course of an eruption is more common than generally acknowledged (Johnson et al., 2008; Brenna et al., 2010). Our study on the deeply eroded SRVF plumbing system indicates that fractionation during ascent and storage in shallow plumbing systems is capable of generating evolved magmas at basaltic monogenetic volcanoes. At SRVF, sills that show evidences of differentiation, i.e., those containing segregated syenite, are relatively thick, 10 – 50 m. According to Jaeger (1957), the time for a mafic intrusion to solidify is proportional to the square of its thickness such as:

$$t \text{ (in years)} = 0.013D^2$$

where D is the intrusion's thickness in meters. Therefore, each individual sill at SRVF would have solidified in 1 to 30 years. A cooling and crystallization model estimates that it would take less

than 4 months for a 10 m thick sill to crystallize down to a 0.35 melt fraction, and less than a year to be completely solid (Diez et al., 2010). Such durations have the same order of magnitude as the duration of some monogenetic eruptions (Johnson et al., 2008) or estimated cooling time of basaltic magma in storage (Mangan, 1990; Vinet and Higgins, 2011) or flood-basalt flows (Philpotts et al., 1996). However, the SRVF mesas observed consist of stacks of sills of various thicknesses. Also, the spacing between individual sills vary from a few meters to hundreds of meters. Consequently, our estimates for cooling time must be regarded as minimum time intervals. The cumulative heat resulting from the overall SRVF intrusions may have persisted for centuries, depending on the number and rate of intrusions, and may have helped maintain solidifying hydrated melts at a relatively high temperature, facilitating porous flow. Nevertheless, our estimates imply that differentiation in individual shallow sills may occur during the course of an eruption whose style may vary from effusive to explosive by tapping different magma compositions. Therefore, it is critical to investigate the occurrence of such segregated melts, as they may be reactivated if the system is perturbed, for example in the case of new magmatic or fluid injections. Explosive eruptions of magnitude similar to those observed at silicic systems have been documented at a few basaltic volcanic systems (e.g., Masaya, Williams, 1983b; Sunset Crater, Alfano et al., 2018; Telocote volcano, Zawacki et al., 2019), and it is thus important to understand the influence of melt evolution in shallow storage systems (Valentine & Gregg, 2008). This is particularly critical for basaltic systems where evolved melts, potentially enriched in volatiles, may generate explosive eruptions. Geophysical measurements at the earth's surface can detect vertical and horizontal displacements of crustal rocks triggered by upper crustal intrusions (Ebmeier et al., 2018; Fournier et al., 2010). The geochemical and petrological record at SRVF may be used to

inform geophysical models and investigations that target distributed volcanic fields around the Colorado Plateau and Basin and Range transition zone.

CONCLUSIONS

The San Rafael subvolcanic field (SRVF) is part of the north-western Transition Zone between the Colorado Plateau and the Basin and Range. The SRVF igneous rocks exhibit both an intraplate geochemical signature, representative of asthenospheric mantle upwelling, and a lithospheric signature inherited from the metasomatized subcontinental lithospheric mantle. Primitive magmas, represented by some basalts, ascended from the asthenosphere-lithosphere boundary with minimal storage in the lithosphere, and experienced significant (> 40%) degrees of fractional crystallization between 50 and 5 km depth. Basalt intruded the upper crust through dikes and sills, where it further crystallized *in-situ*. Syenite formed at the solidification front of partially solidified basalt and was physically segregated due to density differences that allowed the residual liquid to be segregated from the basalt host. This process is supported by the absence of chilled margins between the syenite and the host, and the coarse-grained texture of syenite. Magma characteristics indicate that syenite is less dense than basalt, which confirms that *in-situ* crystallization of basaltic melt in shallow storage systems may promote segregation and remobilization of differentiated hydrated magma, leading to eruptions more explosive than anticipated at basaltic volcanic systems.

ACKNOWLEDGEMENTS

We thank two reviewers, M. Brenna and P. Kempton for their thorough review of this manuscript and their suggestions for improvement before publication. Sampling and analyses were partially supported by the National Science Foundation EAR grant number 0910696 (University of South Florida). P.W., A.G., Z.A., I.S., M.D., and E.G were involved in field work effort and sample collection. A.G., Z.A., I.S., D.K., V.G., and A.A. contributed to sample preparation and analyses. A.G. supervised D.K. (MS thesis) and A.A. (undergrad senior thesis) for major element analyses, microprobe analyses, and thermobarometry. I.S. supervised V.G. (MSc thesis) studies of whole rocks, EPMA and radiogenic isotope analysis. A.G. did the petrogenetic modeling and spatial interpolation of geochemical data. The authors thank Tom Beasley and Richard Walshaw for technical support during EPMA analyses at FCAEM (Miami) and LEMAS (Leeds) facilities, respectively. We thank Jason Harvey and Linda Forbes for support during the column separations and the Sr and Nd isotope analysis in Leeds. All data included in the manuscript are accessible in the supplementary material.

REFERENCES

Alfano, F., Ort, M.H., Pioli, L., Self S., Hanson, S.L., Roggensack, K., Allison, C.M., Amos, R., & Clarke, A.B. (2018). Subplinian monogenetic ic eruption of Sunset Crater, Arizona, USA. *Geological Society of America Bulletin* **131**, 661-674.

Alibert, C., Michard, A., & Albarede, F. (1986). Isotope and trace element geochemistry of Colorado Plateau volcanics. *Geochimica and Cosmochimica Acta* **50**, 2735-2750.

Arculus, R.J., & Gust, D.A. (1995). Regional petrology of the San Francisco Volcanic Field, Arizona, U.S.A.. *Journal of Petrology*, **36**, 827-861.

Arevalo, R., & McDonough, W.F. (2008). Tungsten geochemistry and implications for understanding the Earth's interior. *Earth and Planetary Science Letters* **272,** 656-665.

Ariskin, A.A. (1999). Phase equilibria modeling in igneous petrology: use of COMAGMAT model for simulating fractionation of ferro-basaltic magmas and the genesis of high-alumina basalt. *Journal of Volcanology and Geothermal Research* **90**, 115–162.

Asmerom, Y., & Edwards, R.L. (1995). U-series isotope evidence for the origin of continental basalts. *Earth and Planetary Science Letters* **134,** 1-7.

Audetat, A., Zhang, L., & Huaiwei, N. (2018). Copper and Li diffusion in plagioclase, pyroxenes, olivine and apatite, and consequences for the composition of melt inclusions. *Geochimica and cosmochimica acta* **243,** 99-115.

Ballmer, M.D., Conrad, C.P., Smith, E.I., & Johnsen, R. (2015). Intraplate volcanism at the edges of the Colorado Plateau sustained by a combination of triggered edge-driven convection and shear-driven upwelling. *Geochemistry Geophysics Geosystems* **16**, 366-379.

Beard J. S., Ragland P. C., & Rushmer T. (2004). Hydration crystallization reactions between anhydrous minerals and hydrous melt to yield amphibole and biotite in igneous rocks: description and implications. *Journal of Geology* **112**, 617–621.

Beard, J.S. & Scott, S.R. (2018). A Model for the High-temperature Origin and Paradoxical Distribution of Pegmatites in Mafic Plutons, Smartville Complex, California. *Journal of Petrology* **59**, 3–10.

Berger, J., Lo, K., Diot, H., Triantafyllou, A., Plissart, G., & Féménias, O. (2017). Deformation-driven differentiation during in situ crystallization of the 2.7 Ga Iguilid mafic intrusion (West African Craton, Mauritania). *Journal of Petrology* **58**, 819–840.

Best, M.G. (1970). Kaersutite-peridotite inclusions and kindred megacrysts in basanitic lavas, Grand Canyon, Arizona. *Contributions to Mineralogy and Petrology*, **27**, 25-44.

Bloomfield, A., & Arculus, R. (1989). Magma mixing in the San Francisco Volcanic Field, AZ. *Contributions to Mineralogy and Petrology*, **102**. 10.1007/BF00371086.

Boettcher, A.L., & O'Neil, J.R. (1980). Stable isotope, chemical, and petrographic studies of high-pressure amphiboles and micas: evidence for metasomatism in the mantle source regions of alkali basalts and kimberlites. *American Journal of Science* **280-A**, 594-621.

Brenna, M., Cronin, S.J., Smith, I.E.M., Sohn, Y.K., & Nemeth, K. (2010). Mechanisms driving polymagmatic activity at a monogenetic volcano, Udo, Jeju Island, South Korea. *Contributions to Mineralogy and Petrology* **160**, 931-950.

Burchardt, S. & Galland, O. (2016). Studying Volcanic Plumbing Systems –Multidisciplinary Approaches to a Multifaceted Problem. In: Nemeth, K.(ed.) *Updates in Volcanology. From Volcano Modelling to Volcano Geology.* DOI: 10.5772/63959.

Carman, M.F. (1994). Mechanisms of differentiation in shallow mafic alkaline intrusions, as illustrated in the Big Bend area, western Texas. *Journal of Volcanology and Geothermal Research* **61**, 1-44.

Caroff, M., Ambrics, C., Maury, R., & Cotton, J. (1997). From alkali basalt to phonolite in hand-size samples: vapor-differentiation effects in the Bouzentès lava flow (Cantal, France). *Journal of Volcanology and Geothermal Research* **79**(1–2), 47-61.

Cartwright, J., & Hansen, D.M. (2006). Magma transport through the crust via interconnected sill complexes. *Geology* **34**, 929–932.

Cashman, K.V., Sparks, R.S., & Blundy, J.D. (2017). Vertically extensive and unstable magmatic systems: A unified view of igneous processes. *Science* **355**, 9 p.

Condie, K.C., & Selverstone, J. (1999). The Crust of the Colorado Plateau: New Views of an Old Arc. *Journal of Geology* **107**, 387–397.

Connor, C.B. & Conway, F.M. (2000). Basaltic volcanic fields. In Sigurdsson, H., Houghton, B.F., McNutt, S.R., Rymer, H., & Stix, J. (Eds.), *Encyclopedia of Volcanoes*. Academic Press, 331-343.

Cortés, J.A., Smith, E.I., Valentine, G.A., Johnsen, R., Rasoazanamparany, C., Widom, E., Sas, M., & Ruth, D. (2015). Intrinsic conditions of magma genesis at the Lunar Crater Volcanic Field (Nevada), and implications for internal plumbing and magma ascent. *American Mineralogist* **100**, 396-413.

Cottrell, E., & Kelley, K.A. (2011). The oxidation state of Fe in MORB glasses and the oxygen fugacity of the upper mantle. *Earth and Planetary Science Letters* **305 (**3–4), 270-282.

Crow, R., Karlstrom, K., Asmerom, Y., Schmandt, B., Polyak, V., & DuFrane, S.A. (2011). Shrinking of the Colorado Plateau via lithospheric mantle erosion: Evidence from Nd and Sr isotopes and geochronology of Neogene basalts. *Geology* **39**, 27-30.

Crummy, J., Savov, I.P, Navarro-Ochoa, C., Morgan, D., & Wilson, M. (2014). High-K mafic Plinian eruptions of Volcán de Colima, México. *Journal of Petrology* **55** (10). 1-18.

Delaney, P. & Gartner, A. (1997). Physical processes of shallow mafic dike emplacement near the San Rafael Swell, Utah. *Geological Society of America Bulletin* **109**, 1177-1192.

Diez, M., Connor, C.B., Kruse, S.E., Connor, L., & Savov, I.P. (2009). Evidence of small-volume igneous diapirism in the shallow crust of the Colorado Plateau, San Rafael Desert, Utah. *Lithosphere* **1**, 328-336.

Diez, M., Savov, I., & Connor, C., (2010). Melt segregation in sills in the shallow crust: insights from the San Rafael Swell, Utah. AGU Fall Meeting Abstracts.

Dodson, A., Depaolo, D.J., & Kennedy, B.M. (1998). Helium isotopes in lithospheric mantle: evidence from Tertiary basalts of the Western U.S.A. *Geochimica and cosmochimica Acta* **62**, 3775-3787.

Ebmeier, S.K., Andrews, B.J., Araya, M.C., Arnold, D.W.D., Biggs, J., Cooper, C., Cottrell, E., Furtney, M., Hickey, J., Jay, J., Lloyd, R., Parker, A.L., Pritchard, M.E., Robertson, E., Venzke, E., &

Williamson, J.L. (2018). Synthesis of global satellite observations of magmatic and volcanic deformation: implications for volcano monitoring & the lateral extent of magmatic domains. *Journal of Applied Volcanology* **7**, 1-26.

Esperança, E. Carlson, R.W., & Shirey, S.B. (1988). Lower crustal evolution under central Arizona: Sr, Nd and Pb isotopic and geochemical evidence from the mafic xenoliths of Camp Creek. *Earth and Planetary Science Letters* **90**, 26-40.

Faust, M. (2005). Petrogenesis and geochemistry of Pleistocene and Pliocene flows of the Pine Valley Volcanic Field, Utah and their relationship to the tectonics of the Utah transition zone. UNLV Retrospective Theses & Dissertations. 1827, 141 pp.

Fitton, J.G., James, D., & Leeman, W. (1991). Basic Magmatism Associated With Late Cenozoic Extension in the Western United States: Compositional Variations in Space and Time. *Journal of Geophysical Research* **96**, 13693-13711.

Fournier, T.J., Pritchard, M.E., & Riddick, S.N. (2010). Duration, magnitude, and frequency of subaerial volcano deformation events: New results from Latin America using InSAR and a global synthesis. *Geochemistry, Geophysics, Geosystems*, **11**(1), doi.org/10.1029/2009GC002558.

Gartner, A.E. & Delaney, P.T. (1988). Geologic map showing a late Cenozoic basaltic intrusive complex, Emery, Sevier, and Wayne counties, Utah. *United States Geological Survey,* Map MF-2052.

Genareau, K., Valentine, G.A., Moore, G., & Hervig, R.L. (2010). Mechanisms for transition in eruptive style at a monogenetic scoria cone revealed by microtextural analyses (Lathrop Wells volcano, Nevada, U.S.A.). *Bulletin of Volcanology* **72**, 593-607.

Geshi, N. (2001). Melt segregation by localized shear deformation and fracturing during crystallization of magma in shallow intrusions of the Otoge volcanic complex, central Japan. *Journal of Volcanology and Geothermal Research* **106**, 285-300.

Gibson, S., Thompson, R., Leat, P., Dickin, A., Morrison, M., Hendry, G., & Mitchell, J. (1992). Asthenosphere-derived magmatism in the Rio Grande rift, western USA: Implications for continental break-up. *Geological Society, London, Special Publications* **68**, 61-89.

Gilluly, J. (1927). Analcite diabase and related alkaline syenite from Utah. *The American Journal of Science Series* **5**, 199-211.

Gilluly, J. & Reeside, J.B. (1928). Sedimentary rocks of the San Rafael swell and some adjacent areas in eastern Utah. *United States Geological Survey Professional Paper* **150D**, 61-110.

Giordano, D., Russel, J., & Dingwell, D.B. (2008). Viscosity of magmatic liquids: A model. *Earth and Planetary Science Letters* **271**, 123-134.

Goff, F. (1996). Vesicle cylinders in vapor-differentiated basalt flows. *Journal of Volcanology and Geothermal Research* **71,** 167-185.

Gonzales, D.A., & Lake, E.T. (2016). Geochemical constraints on mantle-melt sources for Oligocene to Pleistocene mafic rocks in the Four Corners region, USA. *Geosphere* **13**, 201-226.

Harp, A.G. & Valentine, G.A. (2015). Shallow plumbing and eruptive processes of a scoria cone built on steep terrain. *Journal of Volcanology and Geothermal Research* **294**, 37-55.

Hartley, M.E., & Thordarson, T. (2009). Melt segregations in a Columbia River Basalt lava flow: A possible mechanism for the formation of highly evolved mafic magmas. *Lithos* **112 (**3–4), 434-446.

Helz, R.T. (1980). Crystallization history of Kilauea Iki lava lake as seen in drill core recovered in 1967–1979. *Bulletin of Volcanology* **434**, 675–701.

Hintz, A.R. & Valentine, G.A. (2012). Complex plumbing of monogenetic scoria cones: New insights from the Lunar Crater Volcanic Field (Nevada, USA). *Journal of Volcanology and Geothermal Research* **239**, 19-32.

Hofmann, A.W. (1997). Mantle geochemistry: The message from oceanic volcanism. *Nature* **358**, 219-229.

Holness, M.B., Nielsen, T. F.D., & Tegner, C. (2017). The Skaergaard Intrusion of East Greenland: Paradigms, Problems and New Perspectives. *Elements* **13**, 391–396.

Humphreys, E.D. (1995). Post-Laramide removal of the Farallon slab, western United States. *Geology* **23**, 987-990.

Hutchison, C.S. (1974). Laboratory handbook of petrographic techniques. John Wiley & Sons, New York.

Iacovino, K. & Till, C.B. (2019). DensityX: A program for calculating the densities of magmatic liquids up to 1,627 °C and 30 kbar. *Volcanica* **2**, 1-10.

Jackson, M.D., Blundy, J., & Sparks, R.S.J. (2018). Chemical differentiation, cold storage and remobilization of magma in the Earth's crust. *Nature* **564**, 405-409.

Jaeger, J.C. (1957). The temperature in the neighborhood of a cooling intrusive sheet. *American Journal of Science* **255**, 306 – 318.

Janoušek, V., Farrow, C. M., & Erban, V. (2006). Interpretation of whole-rock geochemical data in igneous geochemistry: introducing Geochemical Data Toolkit (GCDkit). *Journal of Petrology* **47**, 1255-1259

Jerram, D.A. & Bryan, S.E. (2017). Plumbing systems of shallow level intrusive complexes. In: Breitkreuz C. & Rocchi S. (eds) *Physical Geology of Shallow Magmatic Systems. Advances in Volcanology*, Springer. 39-60.

Jochum, K.P., Nohl, U., Herwig, K., Lammel, E., Stoll, B. & Hofmann, A.W. (2005), GeoReM: A New Geochemical Database for Reference Materials and Isotopic Standards. *Geostandards and Geoanalytical Research*, **29**: 333-338. doi:10.1111/j.1751-908X.2005.tb00904.x

Johnson E.R, Wallace, P., Cashman, K.V., Delgado Granados, & H., Kent, A.J.R. (2008). Magmatic volatile contents and degassing-induced crystallization at Volcán Jorullo, Mexico: Implications for melt evolution and the plumbing systems of monogenetic volcanoes. *Earth and Planetary Science Letters* **269**, 478-487.

Keating, G.N., Valentine, G.A., Krier, D.J., & Perry, F.V. (2008). Shallow plumbing systems for small-volume basaltic volcanoes. *Bulletin of Volcanology* **70**, 563-582.

Kelley, K. A., Plank, T., Ludden, J., & Staudigel, H. (2003). Composition of altered oceanic crust at ODP Sites 801 and 1149. Geochemistry, Geophysics, Geosystems 4(6), 21p.

Kempton, P. D., Fitton, J. G., Hawkesworth, C. J., & Ormerod, D. S. (1991). Isotopic and trace element constraints on the composition and evolution of the lithosphere beneath the southwestern United States, *Journal of Geophysical Research* **96**, 13713– 13735.

Kereszturi, G., Németh, K., Cronin S.J., Agustín-Flores, J., Smith, I.E.M., & Lindsay, J. (2013). A model for calculating eruptive volumes for monogenetic volcanoes — Implication for the Quaternary Auckland Volcanic Field, New Zealand. *Journal of Volcanology and Geothermal Research* **266**, 16-33.

Kiyosugi, K., Connor, C.B., Wetmore, P.H., Ferwerda, B.P., Germa, A.M., Connor, L.J., & Hintz, A.R. (2012). Relationship between dike and volcanic conduit distribution in a highly eroded monogenetic volcanic field: San Rafael, Utah, USA. *Geology* **40**, 695-698.

Lange, R. Frey, H. & Hector, J. (2009). A thermodynamic model for the plagioclase-liquid hygrometer/thermometer. *American Mineralogist* **94**. 494-506.

Langmuir, C.H. (1989). Geochemical consequences of in situ crystallization. *Nature* **340**, 199-205.

Latutrie, B., & Ross, P.S. (2019). Transition zone between the upper diatreme and lower diatreme: origin and significance at Round Butte, Hopi Buttes Volcanic Field, Navajo Nation, Arizona. *Bulletin of Volcanology* **81**(26).

Le Bas, M.J., Le Maitre, R.W., Streckeisen, A, & Zanettin, B. (1986). A chemical classification of volcanic rocks based on the total alkali-silica diagram. *Journal of Petrology* **27**, 745–750.

Lee, C.-T. A., Luffi, P., Plank, T., Dalton, H. A., & Leeman, W. P. (2009). Constraints on the depths and temperatures of basaltic magma generation on Earth and other terrestrial planets using new thermobarometers for mafic magmas. *Earth and Planetary Science Letters* **279**, 20-33.

Lefebvre, N.S., White, J.D.L., & Kjarsgaard, B.A. (2012). Spatter-dike reveals subterranean magma diversions: Consequences for small multivent basaltic eruptions. *Geology* **40**, 423-426.

London, D. & Morgan, G.B. (2012). The Pegmatite Puzzle. *Elements* **8**, 263-268.

Macdonald, R., Smith, R.L., & Thomas, J.E. Jr. (1992). Chemistry of the subalkaline silicic obsidians. *U.S. Geological Survey Professional Paper* 1523, 1-214.

Mangan, M.T. (1990). Crystal size distribution systematics and the determination of magma storage times: The 1959 eruption of Kilauea volcano, Hawaii. *Journal of Volcanology and Geothermal Research* **44,** 295 – 302.

Marsh, B.D. (2002). On bimodal differentiation by solidification front instability in basaltic magmas, part 1: Basic mechanics. *Geochimica et Cosmochimica Acta* **66**, 2211–2229.

Masotta, M., Freda, C. & Gaeta, M. (2012). Origin of crystal-poor, differentiated magmas: insights from thermal gradient experiments. *Contributions to Mineralogy and Petrology* **163**, 49–65.

McDonough, W.F. (1990). Constraints on the composition of the continental lithospheric mantle. *Earth and Planetary Science Letters* **101**, 1-18.

Morgan, G.B. & London, D. (1999). Crystallization of the Little Three layered pegmatite-aplite dike, Ramona District, California. *Contributions to Mineralogy and Petrology* **136**, 310-330.

Muirhead, J.D., Van Eaton, A.R., Re, G., White, J.D.L., & Ort, M.H. (2016). Monogenetic volcanoes fed by interconnected dikes and sills in the Hopi Buttes volcanic field, Navajo Nation, USA. *Bulletin of Volcanology* **78**, 11. https://doi.org/10.1007/s00445-016-1005-8.

Murray, R.W., Miller, D.J., & Kryc, K.A. (2000). Analysis of major and trace elements in rocks, sediments, and interstitial waters by inductively coupled plasma–atomic emission spectrometry (ICP-AES). ODP Technical Note 29, http://www-odp.tamu.edu/ publications/tnotes/tn29/INDEX.HTM.

Nakamura, N. (1974). Determination of REE, Ba, Fe, Mg, Na, and K in Carbonaceous and Ordinary Chondrites. *Geochimica et Cosmochimica Acta* **38**, 757-775.

Pankhurst, M., Walshaw, R, & Morgan, D.J. (2016). Major Element Chemical Heterogeneity in Geo2 Olivine Microbeam Reference Material: A Spatial Approach to Quantifying Heterogeneity in Primary Reference Materials. *Geostandards and Geoanalytical Research* **41** (1), 85 – 91.

Philpotts, A.R., Carroll, M., & Hill, J.M. (1996). Crystal-mush compaction and the origin of pegmatitic segregation sheets in a thick flood-basalt flow in the Mesozoic Hartford Basin, Connecticut. *Journal of Petrology* **37** (4), 811-836.

Plank, T.A., & Forsyth, D.W. (2016) Thermal structure and melting conditions in the mantle beneath the Basin and Range Province from seismology and petrology. *Geochemistry, Geophysics, Geosystems* **17**, 1312-1338.

Planke S., Svensen H., Myklebust R., Bannister S., Manton B., & Lorenz L. (2017). Geophysics and Remote Sensing. In: Breitkreuz C., & Rocchi, S. (eds) *Physical Geology of Shallow Magmatic Systems. Advances in Volcanology*. Springer, 131-146.

Puffer, J.H., & Horter, D.L. (1993). Origin of pegmatitic segregation veins within flood basalts. *Geological Society of America Bulletin* **105** (6), 738–748.

Putirka, K.D. (2005). Igneous thermometers and barometers based on plagioclase + liquid equilibria: Tests of some existing models and new calibrations. *American Mineralogist* **90**, 336–346.

Putirka, K.D. (2008). Thermometers and barometers for volcanic systems. In: Putirka, K. D., and Tepley, F. (eds.). *Reviews in Mineralogy and Geochemistry* **69**, 61-120.

Putirka, K.D., Johnson, M., Kinzler, R., & Walker, D., (1996). Thermobarometry of mafic igneous rocks based on clinopyroxene-liquid equilibria, 0-30 kbar. *Contributions to Mineralogy and Petrology* **123**, 92-108.

Re, G., Palin, J.M., White, J.D.L., & Parolari, M. (2017). Unravelling the magmatic system beneath a monogenetic volcanic complex (Jagged rocks complex, Hopi Buttes, Az, U.S.A.). *Contributions to Mineralogy and Petrology* **172** (94).

Reid, M.R., Bouchet, R.A., Blichert-Toft, J., Levander, A., Liu, K., Miller, M.S., & Ramos, F.C. (2012). Melting under the Colorado Plateau, USA. *Geology* **40**, 387-390.

Reid, M.R., & Ramos, F.C. (1996). Chemical dynamics of enriched mantle in the southwestern U.S.: Thorium isotope evidence. *Earth and Planetary Science Letters* **138**, 67–81.

Richardson, J.A., Connor, C.B., Wetmore, P.H., Connor, L.J., Gallant, E.A. (2015). Role of sills in the development of volcanic fields: Insights from lidar mapping surveys of the San Rafael Swell, Utah. *Geology* **43**, 1023-1026.

Robinson, J.A.C., & Wood, B.J. (1998). The depth of the spinel to garnet transition at the peridotite solidus. *Earth and Planetary Science Letters* **164 (**1–2), 277-284.

Rocchi S. & Breitkreuz C. (2017) Physical Geology of Shallow-Level Magmatic Systems—An Introduction. In: Breitkreuz, C. & Rocchi, S. (eds). *Physical Geology of Shallow Magmatic Systems. Advances in Volcanology*. Springer, pp: 1-10.

Roden, M. F., Smith, D., & Murthy, V. R. (1990). Chemical constraints on lithosphere composition and evolution beneath the Colorado Plateau. *Journal of Geophysical Research* **95**(B3), 2811– 2831.

Rowe, M.C., & Lassiter, J.C. (2009). Chlorine enrichment in central Rio Grande rift basaltic melt inclusions: Evidence for subduction modification of the lithospheric mantle. *Geology* **37**, 439-442.

Rowe, M.C., Lassiter, J.C., & Goff, K. (2015). Basalt volatile fluctuations during continental rifting: an example from the Rio Grande rift, U.S.A. *Geochemistry, Geophysics, Geosystems* **16**, 1254-1273.

Rudzitis, S., Reid M. R., & Blichert-Toft J. (2016). On edge melting under the Colorado Plateau margin, *Geochemistry Geophysics Geosystems* **17**, 2835–2854.

Schandl, E.S. & Gorton, M.P. (2002). Application of high field strength elements to discriminate tectonic settings in VMS environments. *Economic Geology* **97**, 629-642.

Seropian, G., Rust, A. C., & Sparks, R. S. J. (2018). The gravitational stability of lenses in magma mushes: Confined Rayleigh-Taylor instabilities. *Journal of Geophysical Research: Solid Earth* **123,** 3593– 3607.

Shane, P., & Coote, A. (2018). Thermobarometry of Whangarei volcanic field lavas, New Zealand: Constraints on plumbing systems of small monogenetic volcanoes. *Journal of Volcanology and Geothermal Research* **354**, 130-139.

Smith, R.L., & Luedke, R.G. (1984). Potentially active volcanic lineaments and loci in western conterminous United States. in *Explosive Volcanism: Inception, Evolution, and Hazards: Washington, D.C., National Academy Press, Studies in Geophysics*, pp. 47–66.

Sun, S.S. & McDonough, W.F. (1989). Chemical and isotopic systematics of oceanic basalts: implications for mantle composition and processes. In: Saunders, A.D. & Norry, M (eds). *Magmatism in the ocean basins. Geological Society of London Special Publications* **42**, 313–345.

Thomson, K. & Schofield, N. (2008). Lithological and structural controls on the emplacement and morphology of sills in sedimentary basins. *Geological Society, London, Special Publications* **302**, 31-44.

Thompson, G. A. & Zoback, M. L. (1979). Regional geophysics of the Colorado Plateau. *Tectonophysics* **61**, 149–181.

Tingey, D.G., Christiansen, E.H., Best, M.G., Ruiz, J., & Lux, D.R. (1991). Tertiary Minette and Melanephelinite Dikes, Wasatch Plateau, Utah: Records of Mantle Heterogeneities and Changing Tectonics. *Journal of Geophysical Research* **96**, 13529-13544.

Valentine, G.A. & Cortés, J.A. (2013). Time and space variations in magmatic and phreatomagmatic eruptive processes at Easy Chair (Lunar Crater Volcanic Field, Nevada, USA). *Bulletin of Volcanology* **75**, 752. https://doi.org/10.1007/s00445-013-0752-z.

Valentine, G.A. & Gregg, T.K.P. (2008). Continental basaltic volcanoes — Processes and problems. *Journal of Volcanology and Geothermal Research* **17**, 857-873.

Vinet, N. & Higgins, M.D. (2011). What can crystal size distributions and olivine compositions tell us about magma solidification processes inside Kilauea Iki lava lake, Hawaii? *Journal of Volcanology and Geothermal Research* **208**, 136-162.

Wang, K., Plank, T., Walker, J. D., & Smith, E. I. (2002). A mantle melting profile across the Basin and Range, SW USA. *Journal of Geophysical Research* **107**. https://doi.org/10.1029/2001JB000209.

Weis, D., Kieffer, B., Maerschalk, C., Barling, J.,D., Jong, J., Williams, G. A.Hanano, D., Pretorius, W., Mattielli, N.,Scoates, J. S., Goolaerts, A., Friedman, R. M., & Mahoney, J.B. (2006). High-precision

isotopic characterization of USGS reference materials by TIMS and MC-ICP-MS. *Geochemistry, Geophysics, Geosystems* **7**, 1-30.

Williams, J.D. (1983a). The petrography and differentiation of a composite sill from the San Rafael swell region, Utah. Arizona State University, Thesis (M.S.). 133 pp.

Williams, S.N. (1983b) Plinian airfall deposits of basaltic composition. *Geology* **11**, 211-214.

Workman, R.K. & Hart, S.R. (2005). Major and trace element composition of the depleted MORB mantle (DMM). *Earth and Planetary Science Letters* **231**, 53-72.

Zavala, K., Leitch, A.M., & Fisher, G.W. (2011). Silicic Segregations of the Ferrar Dolerite Sills, Antarctica. *Journal of Petrology* **52**, 1927-1964.

Zawacki, E.E., Clarke, A.B., Arrowsmith, J.R., Bonadonna, C., & Lynch, D.J. (2019). Tecolote volcano, Pinacate volcanic field (Sonora, Mexico): A case of highly explosive basaltic volcanism and shifting eruptive styles. *Journal of Volcanology and Geothermal Research* **379**, 23-44.

Zindler A, & Hart S. (1986). Chemical Geodynamics. *Annual Review of Earth & Planetary Sciences* **14**, 493-571.

FIGURE CAPTIONS

Figure 1: Geologic setting of the San Rafael subvolcanic field (SRVF). (a) Simplified map of the south-western United States showing extent of the Colorado Plateau (grey line), location of Quaternary intraplate volcanism in the northern and southern transition zone between the Colorado Plateau and the Basin and Range Province. SRVF is located in red. US states are labelled by their acronyms: Idaho (ID), Wyoming (WY), Nevada (NV), Utah (UT), Colorado (CO), California (CA), Arizona (AR), New Mexico (NM). (b) Digital Elevation Model (DEM) and simplified geologic map of the SRVF (modified from Gartner & Delaney, 1988; Kiyosugi et al., 2012) showing mapped sills, dikes, and conduits. Main sills and other geographic areas cited in the text and tables are located by their acronyms on the map: Hebes Sill (HS), Bad Luck sill (BL), Cedar Mountain (CM), Moroni Buttes (MB), Frying Pan (FP), Gypsum Springs (GS), Solomon Temple (ST), and Little Black Mountain (LBM). (c) Sample locations. Black symbols are for basalts in sills, red symbols are for syenites in sills, green symbols are for basalts in dikes, blue symbols are for basalt in conduits, and orange symbols are for syenite in conduits.

Figure 2: (a) Typical vertical section (about 30 m tall) showing internal structure of a sill (modified from Williams, 1983a). Basalt is in white, syenite is in grey. Bold lines between Entrada sandstone and basalt represent chilled margins (C.M.). Dashed lines within basalt and between basalt and syenite sheets represent gradational contacts (G.C.). (b) Outcrop scale features showing syenite segregation in basalt in the form of globules. (c) Outcrop scale features showing syenite segregation in basalt in the form of veins. (d) Hand sample of basalt. (e) Hand sample of syenite. (f) Typical sample-scale features of basalt and syenite gradational contact.

Figure 3: Representative photomicrographs of basalt and syenite under polarized light (left column) and crossed-polars (right column) of (a-b) basalt, (c-d) syenite, (e-f) syenite globule in basalt, (g-h) partially serpentinized olivine , (i-j) completely serpentinized olivine , and (k-l) sieved pyroxene. Abbreviations for mineral names: olivine (Ol), diopside (Di), plagioclase (Pl), amphibole (Amp), biotite (Bt), sanidine (San), magnetite (Mag).

Figure 4: Composition of minerals analyzed by electron microprobe. (a) Feldspar classification. (b) Pyroxene classification. Colors represent rock types: basalt samples are in black, syenite samples are in red.

Figure 5 : Total alkali versus silica classification diagram Le Bas et al. (1986) for the SRVF samples. Symbols represent the different geographic groups that correspond to the main sill complexes or dike regions (see sample locations and legend on Figure 1c). Analytical error is smaller than symbol size. Colors represent rock types: black symbols are for basalts in sills, red symbols are for syenites in sills, green symbols are for basalts in dikes, blue symbols are for basalt in conduits, and orange symbols are for syenite in conduits.

Figure 6: (a) Geotectonic classification plot (Schandl and Gordon, 2002) of Th (ppm) vs. Ta (ppm) showing that the SRVF samples cross the fields of within plate volcanic fields and active continental margins. Grey symbols represent the average regional total (TC), upper (UC), and

lower (LC) crust (Condie & Selverstone, 1999), the Sub-Continental Lithospheric Mantle (SCLM, spinel peridotite from McDonough, 1990), and average OIB (Sun & McDonough, 1989). (b) Nb (ppm) vs. La (ppm) plot of SRVF samples. All samples have Nb/La ratios < 1.1 indicating a lithospheric influence (Fitton et al., 1991; Faust, 2005). Symbols and colors same as figure 1. Analytical error is smaller than symbol size. Pale yellow field represents compositions from volcanic fields of the Southern Transition zone (STZ), pale orange represents compositions from San Francisco volcanic field (SFVF), and orange field compositions form the Northern Transition Zone (NTZ). Data for other fields collected from Georoc in June 2020 (Best, 1970; Boettcher & O'Neil, 1980, Alibert et al., 1986, Bloomfield & Arculus, 1989, Gibson et al., 1992, Macdonald et al., 1992, Arculus & Gust, 1995, Asmerom & Edwards, 1995, Dodson et al., 1998; Arevalo & McDonough, 2008; Rowe & Lassiter, 2009; Crow 2011, Rowe et al., 2015, Rudzitis et al., 2016, Plank & Forsyth, 2016, Re et al., 2017, Audetat et al., 2018, Latutrie & Ross, 2019).

Figure 7: Multi-element diagrams normalized to (a) chondrite (Nakamura, 1974), and (b) Primitive Mantle (Sun & McDonough, 1989) values. Black symbols are for basalts, red symbols are for syenites, green line is for OIB (Sun & McDonough, 1989).

Figure 8: (a) Location of samples analyzed for $^{87}Sr/^{86}Sr$ and their isotopic ratio range. (b) Location of samples analyzed for $^{143}Nd/144Nd$ and their isotopic ratio range. (c) $^{143}Nd/^{144}Nd$ versus $^{87}Sr/^{86}Sr$ diagram showing the relation of the SRVF igneous rocks (black and red circles for basalts and syenites, respectively, analytical error smaller than symbol size) to the mantle reservoirs as defined by Zindler and Hart (1986). Country rocks that contain the SRVF intrusions

have been analyzed in this study and are also plotted: Entrada sandstone (orange square) and Curtis formation (yellow square). Bulk Silicate Earth values from Workman and Hart (2005). Also shown are the arrays defined by other volcanic fields of the transition zone between the Colorado Plateau and the Basin and Range province (Fig. 1), data downloaded from Georoc website (http://georoc.mpch-mainz.gwdg.de/) on 11/08/2019 and reported in supplementary table EA11: the Navajo volcanic field (Alibert et al., 1986; Roden et al., 1990; Kempton et al., 1991; Gibson et al., 1992), the Southern transition zone from Arizona to New Mexico (Alibert et al., 1986; Kempton et al., 1991; Crow et al., 2011), the San Francisco Volcanic field (Alibert et al., 1986; Bloomfield & Arculus, 1989; Kempton et al., 1991), and the northern transition zone in Utah (Reid & Ramos, 1996). Grey area for crust defined by data from Esperança et al., 1988.

Figure 9: Temperature (°C) versus Pressure (kbar) and depth (km) from basalt (black) and syenite (red), calculated with the clinopyroxene-liquid thermobarometer of Putirka (2008) using clinopyroxene major element data and whole-rock major element compositions analyzed by EPMA and ICP-OES, respectively. Histogram of depths shows that basalt crystallizes over a broad range of pressures and temperatures as melts ascend through the lithosphere, with a majority of crystals forming between 30 and 22 km depth. Syenite crystallizes in the upper 4 km of the crust (Phanerozoic sediments) where intrusions have transitioned from dikes to sills (Richardson et al., 2015).

Figure 10: Geospatial distribution maps of trace element ratios in basalts obtained by Inverse Distance Weighting Interpolation in ArcGIS10. White circles show location of input data points. (a) ratio of Ba/Ta, (b) ratio of Nb/Ta

Figure 11: Representative major element modeling in COMAGMAT-3 program using CM-10 composition as initial liquid composition, and selecting decompression between 10 and 0.5 kbar, an open system with a QFM+1 oxygen buffer, and 1 – 3 wt. % of water. Equilibrium crystallization models are the bold orange lines. Fractional crystallization models are the dashed purple lines. Crosses are placed at 10% vol. crystallization intervals. Analytical error is smaller than symbol size.

Figure 12: Conceptual model of the SRVF intrusions and magma differentiation by in-situ crystallization and progression of the solidification front. (a) SRVF melts ascend from the asthenosphere-lithosphere boundary then intruded the crust. Model of mantle and crust beneath the western transition zone of the Colorado Plateau adapted from Thompson & Zoback, 1979. (b) Sills intrude the San Rafael group, particularly the Entrada sandstone and Curtis formation, between 4 and 1 km below the surface. Sill thickness exaggerated to show segregation of syenite in basalt. (c) In-situ crystallization of basalt allows the formation and segregation of syenite by crystal mush compaction. The density contrast at relatively low viscosity allows syenite to percolate through the crystal mush and be remobilized into veins, lenses, and sheets.

Table 1: Isotopic data for SRVF igneous rocks and country rocks.

Table 2: Representative mineral mode in basalt and syenite.

ELECTRONIC APPENDICES

EA1: Sample names, sample locations in UTM zone 12, name of main mesa or geographic area, rock type, type of intrusive feature, degree of weathering, and mineral mode.

EA2: Values measured for internal standard JB-3 during major and trace element analyses and expected values for internal (JB-3) and calibration standards (BCR-2, STM-1, JA-2, JP-1, JR-1, W-2, JB-3, BIR-1, and BHVO-2) from GeoReM (Jochum et al., 205).

EA3: Whole-rock major element data, loss on ignition (LOI), calculated mg#, calculated CIPW norm (in norm. mass %) with hornblende and biotite (Hutchison, 1974) processed using GCDKit software (Janoušek et al., 2006). See text for details on calculations.

EA4: Whole-rock trace element data, with calculated ratios used in the text and interpolation for geochemical maps.

EA5: Major element analyses of feldspars, analyzed with electron probe micro-analyzer, with calculated An-Ab-Or values. Facilities used are Florida Center for Analytical Electron Microscopy at Florida International University (FCAEM FIU) and Leeds Electron Microscopy and Spectroscopy Centre at Leeds University (LEMAS).

EA6: Major element analyses of pyroxene, analyzed with electron probe micro-analyzer, with calculated Mg# and En-Wo-Fs values, and temperature (°C) and pressure (kbar) calculated using Putirka (2008) clinopyroxene-liquid thermobarometer. Facilities used are Florida Center for

Analytical Electron Microscopy at Florida International University (FCAEM FIU) and Leeds Electron Microscopy and Spectroscopy Centre at Leeds University (LEMAS).

EA7: Major element analyses of amphibole, biotite, and oxides, analyzed with an electron probe micro-analyzer at Florida Center for Analytical Electron Microscopy at Florida International University (FCAEM FIU).

EA8: Major element analyses of olivine, analyzed with an electron probe micro-analyzer, with calculated Mg# values, and mantle temperature (°C) calculated using Putirka (2008) olivine-liquid thermometer. Facilities used are Florida Center for Analytical Electron Microscopy at Florida International University (FCAEM FIU) and Leeds Electron Microscopy and Spectroscopy Centre at Leeds University (LEMAS).

EA9: Results from the petrogenetic modeling of Equilibrium crystallization (EC) and Fractional Crystallization (FC) using COMAGMAT-3 program.

EA10: Density (g/cc) and viscosity (Pa.s) results for all samples, calculated with DensityX (Iacovino & Till, 2019, https://densityx.herokuapp.com) and grdViscosity (Giordano et al., 2008), respectively.

EA11: $^{143}Nd/^{144}Nd$ and $^{87}Sr/^{86}Sr$ isotopic ratios reported for some other regions of the transition zone between the Colorado Plateau and the Basin and Range that are colored in Fig. 1a: the Navajo volcanic field (Alibert et al., 1986; Roden et al., 1990; Kempton et al., 1991; Gibson et al., 1992), the Southern transition zone from Arizona to New Mexico (Alibert et al., 1986; Kempton et al., 1991; Crow et al., 2011), the San Francisco Volcanic field (Alibert et al., 1986; Bloomfield & Arculus, 1989; Kempton et al., 1991), and the northern transition zone in Utah

(Reid & Ramos, 1996). Values downloaded from GEOROC (http://georoc.mpch-mainz.gwdg.de/) on 11/08/2019 and reported in supplementary table EA11.

FIGURE 1

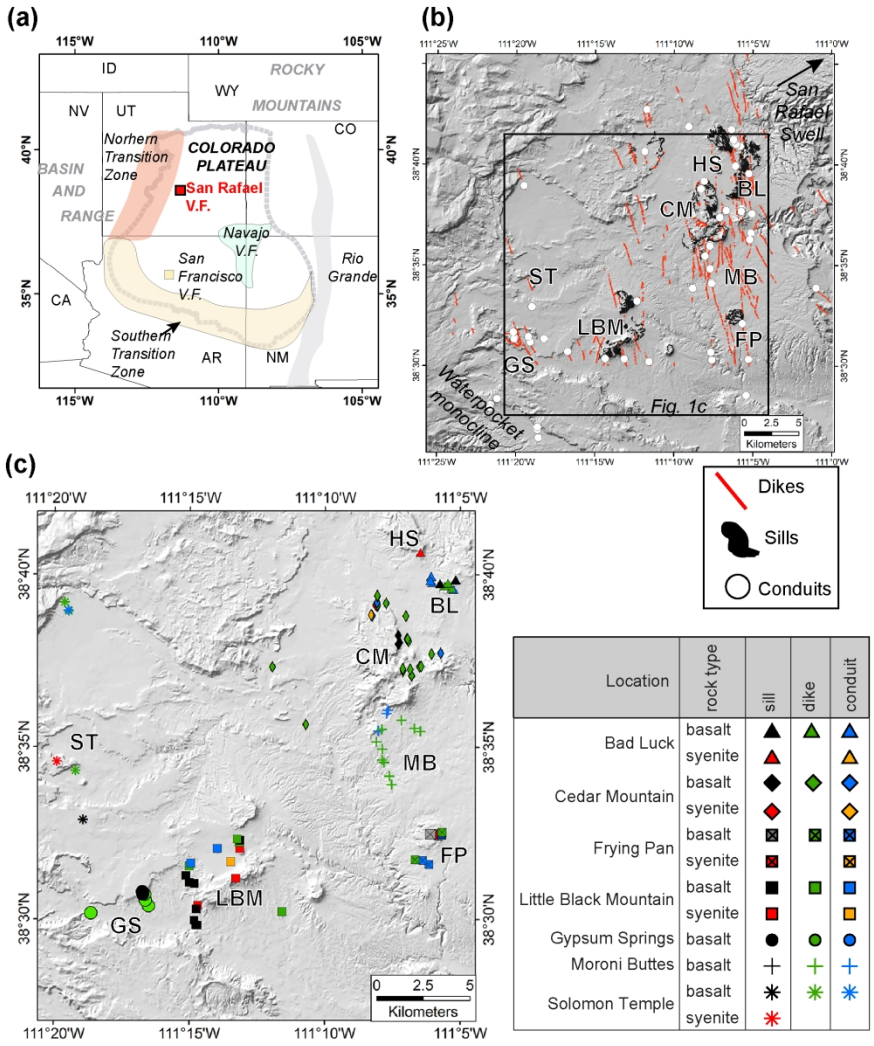

Location	rock type	sill	dike	conduit
Bad Luck	basalt	▲	▲	▲
	syenite	▲		▲
Cedar Mountain	basalt	◆	◆	◆
	syenite	◆		◆
Frying Pan	basalt	⊠	⊠	⊠
	syenite	⊠		⊠
Little Black Mountain	basalt	■	■	■
	syenite	■		■
Gypsum Springs	basalt	●	●	●
Moroni Buttes	basalt	+	+	+
Solomon Temple	basalt	✱	✱	✱
	syenite	✱		

Figure 1: Geologic setting of the San Rafael subvolcanic field (SRVF). (a) Simplified map of the south-western United States showing extent of the Colorado Plateau (grey line), location of Quaternary intraplate volcanism in the northern and southern transition zone between the Colorado Plateau and the Basin and Range Province. SRVF is located in red. US states are labelled by their acronyms: Idaho (ID), Wyoming (WY), Nevada (NV), Utah (UT), Colorado (CO), California (CA), Arizona (AR), New Mexico (NM). (b) Digital Elevation Model (DEM) and simplified geologic map of the SRVF (modified from Gartner & Delaney, 1988; Kiyosugi et al., 2012) showing mapped sills, dikes, and conduits. Main sills and other geographic areas cited in the text and tables are located by their acronyms on the map: Hebes Sill (HS), Bad Luck sill (BL), Cedar Mountain (CM), Moroni Buttes (MB), Frying Pan (FP), Gypsum Springs (GS), Solomon Temple (ST), and Little Black Mountain (LBM). (c) Sample locations. Black symbols are for basalts in sills, red symbols are for syenites in sills, green symbols are for basalts in dikes, blue symbols are for basalt in conduits, and orange symbols are for syenite in conduits.

FIGURE 2

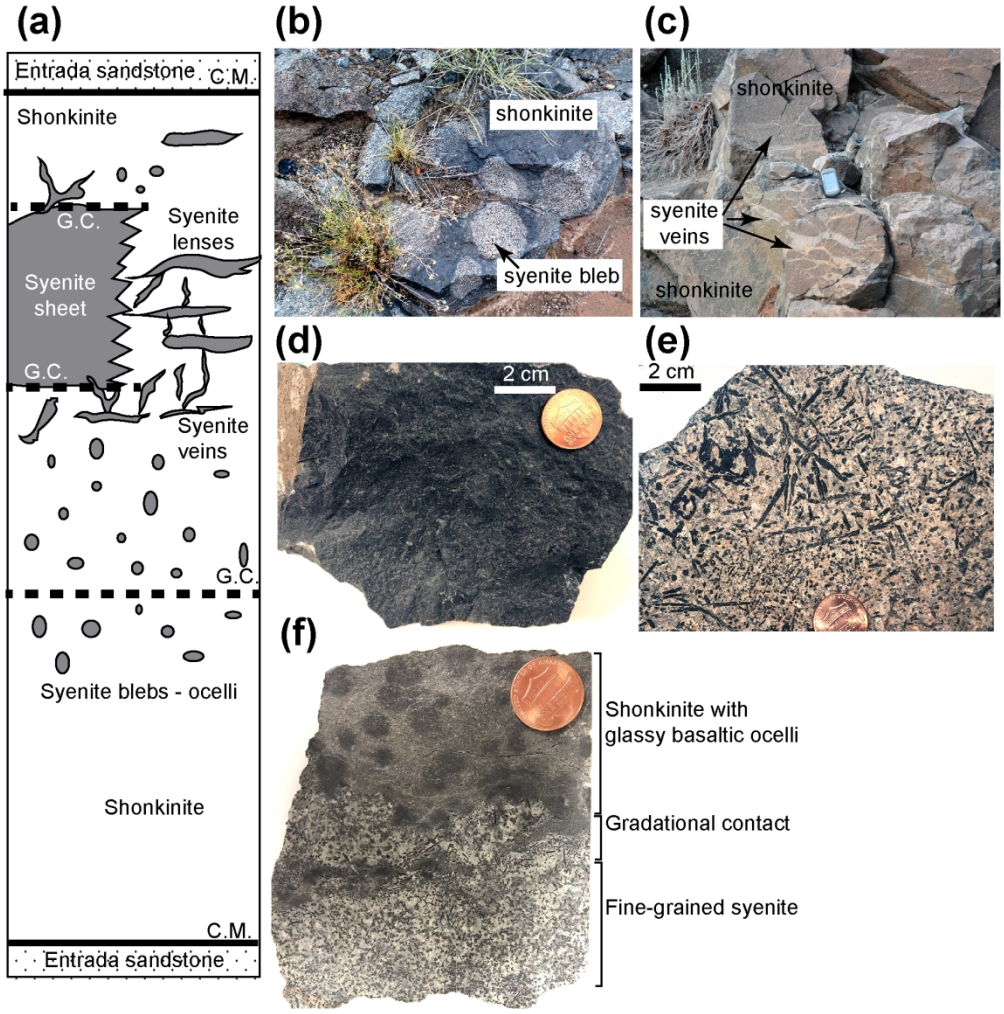

Figure 2: (a) Typical vertical section (about 30 m tall) showing internal structure of a sill (modified from Williams, 1983a). Basalt is in white, syenite is in grey. Bold lines between Entrada sandstone and basalt represent chilled margins (C.M.). Dashed lines within basalt and between basalt and syenite sheets represent gradational contacts (G.C.). (b) Outcrop scale features showing syenite segregation in basalt in the form of globules. (c) Outcrop scale features showing syenite segregation in basalt in the form of veins. (d) Hand sample of basalt. (e) Hand sample of syenite. (f) Typical sample-scale features of basalt and syenite gradational contact.

FIGURE 3-1

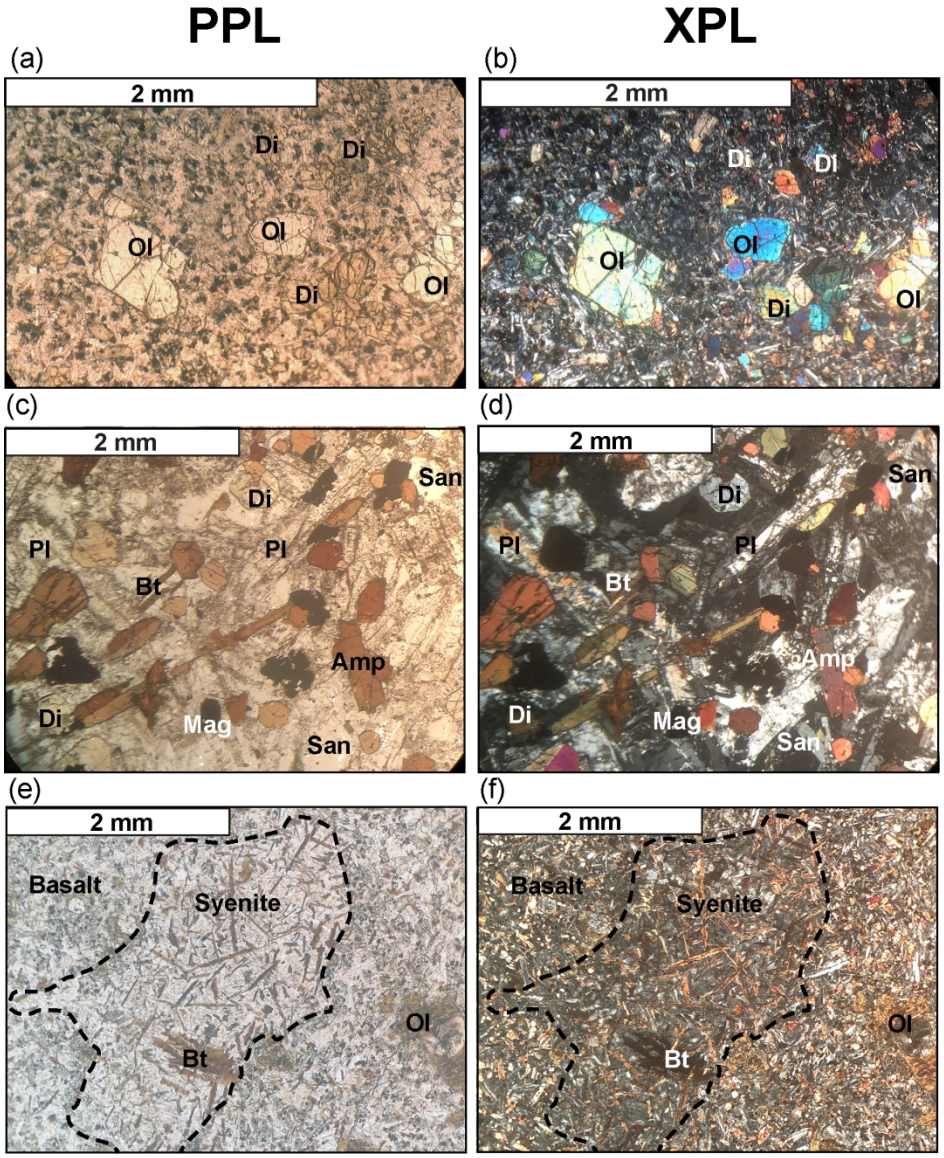

Figure 3-1 (a to f): Representative photomicrographs of basalt and syenite under polarized light (left column) and crossed-polars (right column) of (a-b) basalt, (c-d) syenite, (e-f) syenite globule in basalt, (g-h) partially serpentinized olivine , (i-j) completely serpentinized olivine , and (k-l) sieved pyroxene. Abbreviations for mineral names: olivine (Ol), diopside (Di), plagioclase (Pl), amphibole (Amp), biotite (Bt), sanidine (San), magnetite (Mag).

FIGURE 3-2

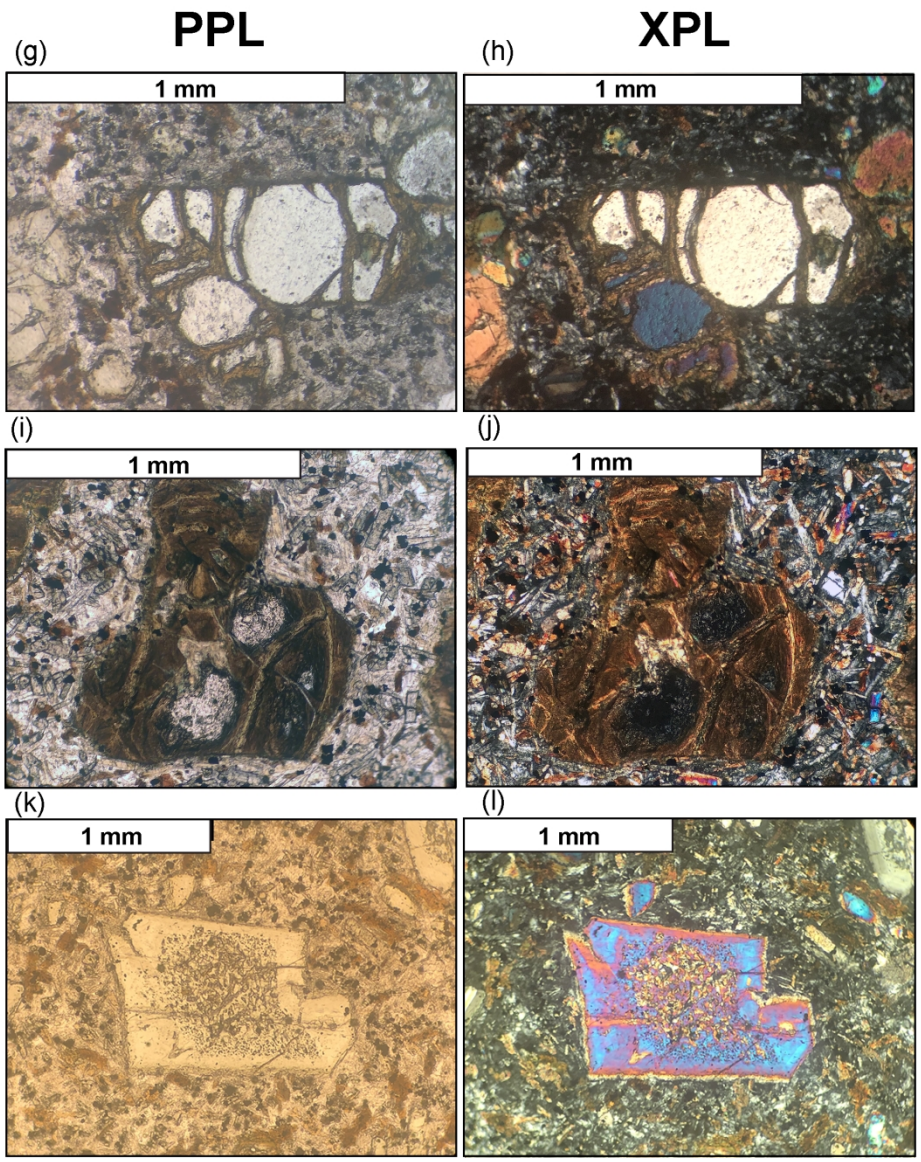

Figure 3-2 (g to l): Representative photomicrographs of basalt and syenite under polarized light (left column) and crossed-polars (right column) of (a-b) basalt, (c-d) syenite, (e-f) syenite globule in basalt, (g-h) partially serpentinized olivine , (i-j) completely serpentinized olivine , and (k-l) sieved pyroxene. Abbreviations for mineral names: olivine (Ol), diopside (Di), plagioclase (Pl), amphibole (Amp), biotite (Bt), sanidine (San), magnetite (Mag).

FIGURE 4

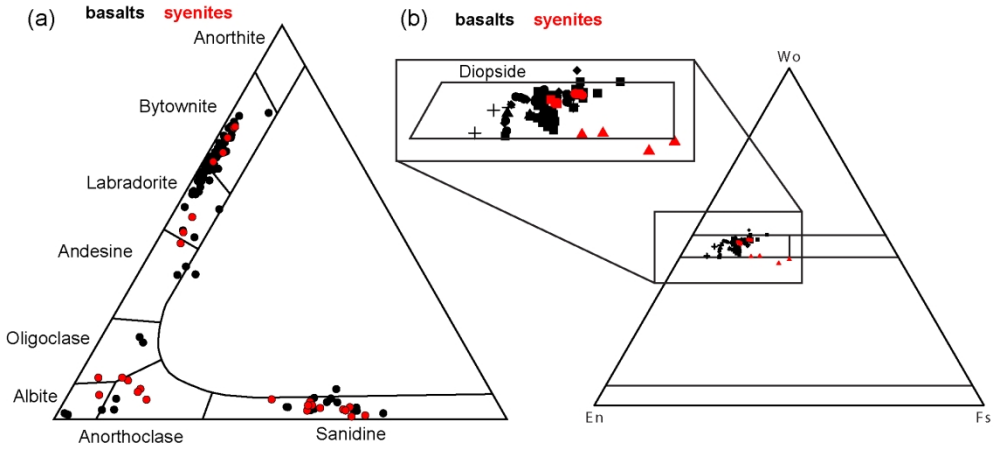

Figure 4: Composition of minerals analyzed by electron microprobe. (a) Feldspar classification. (b) Pyroxene classification. Colors represent rock types: basalt samples are in black, syenite samples are in red.

FIGURE 5

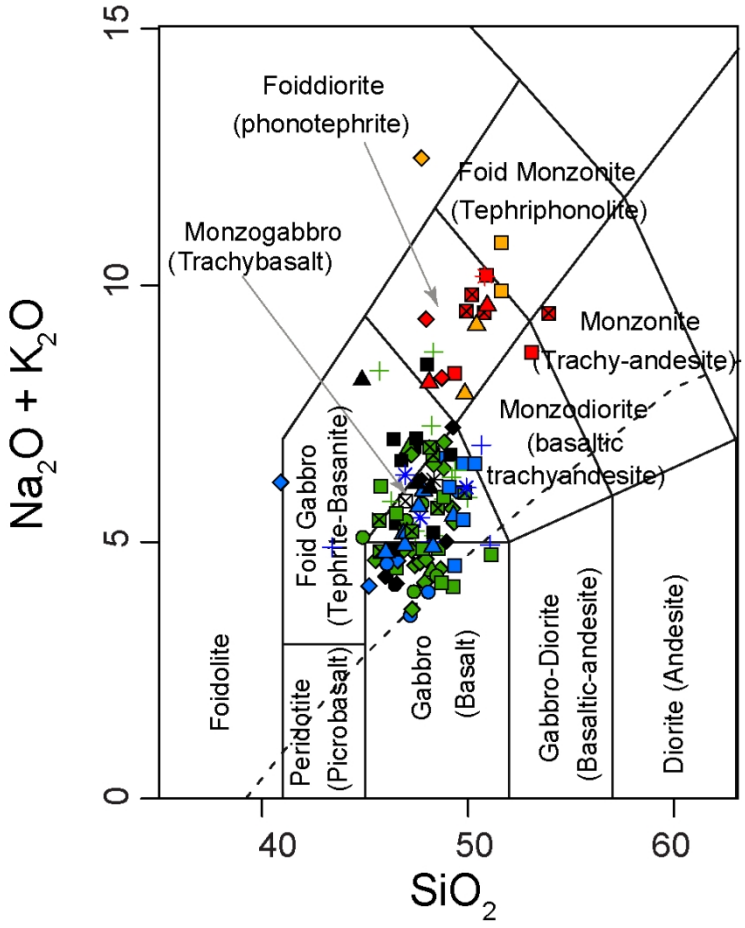

Figure 5 : Total alkali versus silica classification diagram Le Bas et al. (1986) for the SRVF samples. Symbols represent the different geographic groups that correspond to the main sill complexes or dike regions (see sample locations and legend on Figure 1c). Analytical error is smaller than symbol size. Colors represent rock types: black symbols are for basalts in sills, red symbols are for syenites in sills, green symbols are for basalts in dikes, blue symbols are for basalt in conduits, and orange symbols are for syenite in conduits.

FIGURE 6

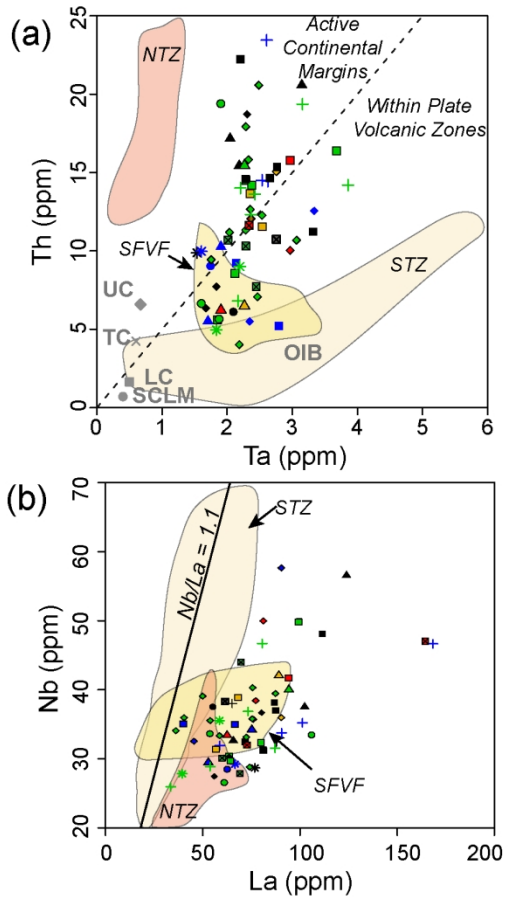

Figure 6:(a) Geotectonic classification plot (Schandl and Gordon, 2002) of Th (ppm) vs. Ta (ppm) showing that the SRVF samples cross the fields of within plate volcanic fields and active continental margins. Grey symbols represent the average regional total (TC), upper (UC), and lower (LC) crust (Condie & Selverstone, 1999), the Sub-Continental Lithospheric Mantle (SCLM, spinel peridotite from McDonough, 1990), and average OIB (Sun & McDonough, 1989). (b) Nb (ppm) vs. La (ppm) plot of SRVF samples. All samples have Nb/La ratios < 1.1 indicating a lithospheric influence (Fitton et al., 1991; Faust, 2005). Symbols and colors same as figure 1. Analytical error is smaller than symbol size. Pale yellow field represents compositions from volcanic fields of the Southern Transition zone (STZ), pale orange represents compositions from San Francisco volcanic field (SFVF), and orange field compositions form the Northern Transition Zone (NTZ). Data for other fields collected from Georoc in June 2020 (Best, 1970; Boettcher & O'Neil, 1980, Alibert et al., 1986, Bloomfield & Arculus, 1989, Gibson et al., 1992, Macdonald et al., 1992, Arculus & Gust, 1995, Asmerom & Edwards, 1995, Dodson et al., 1998; Arevalo & McDonough, 2008; Rowe & Lassiter, 2009; Crow 2011, Rowe et al., 2015, Rudzitis et al., 2016, Plank & Forsyth, 2016, Re et al., 2017, Audetat et al., 2018, Latutrie & Ross, 2019).

FIGURE 7

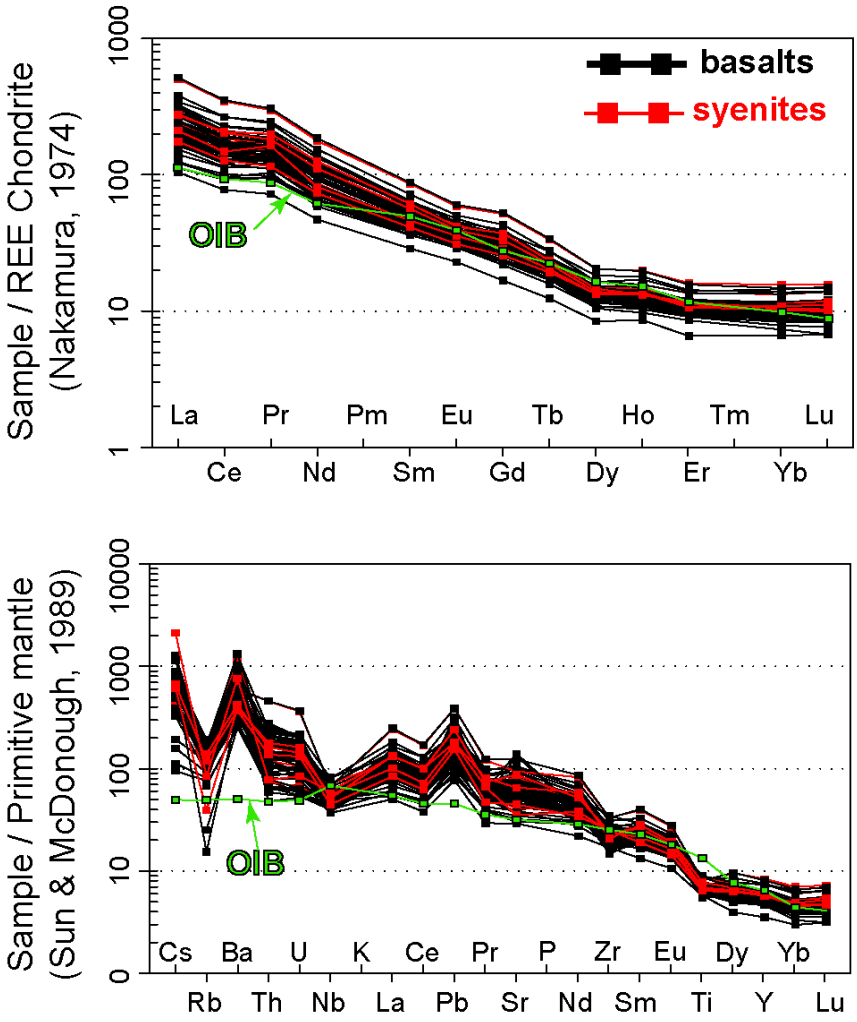

Figure 7: Multi-element diagrams normalized to (a) chondrite (Nakamura, 1974), and (b) Primitive Mantle (Sun & McDonough, 1989) values. Black symbols are for basalts, red symbols are for syenites, green line is for OIB (Sun & McDonough, 1989).

FIGURE 8

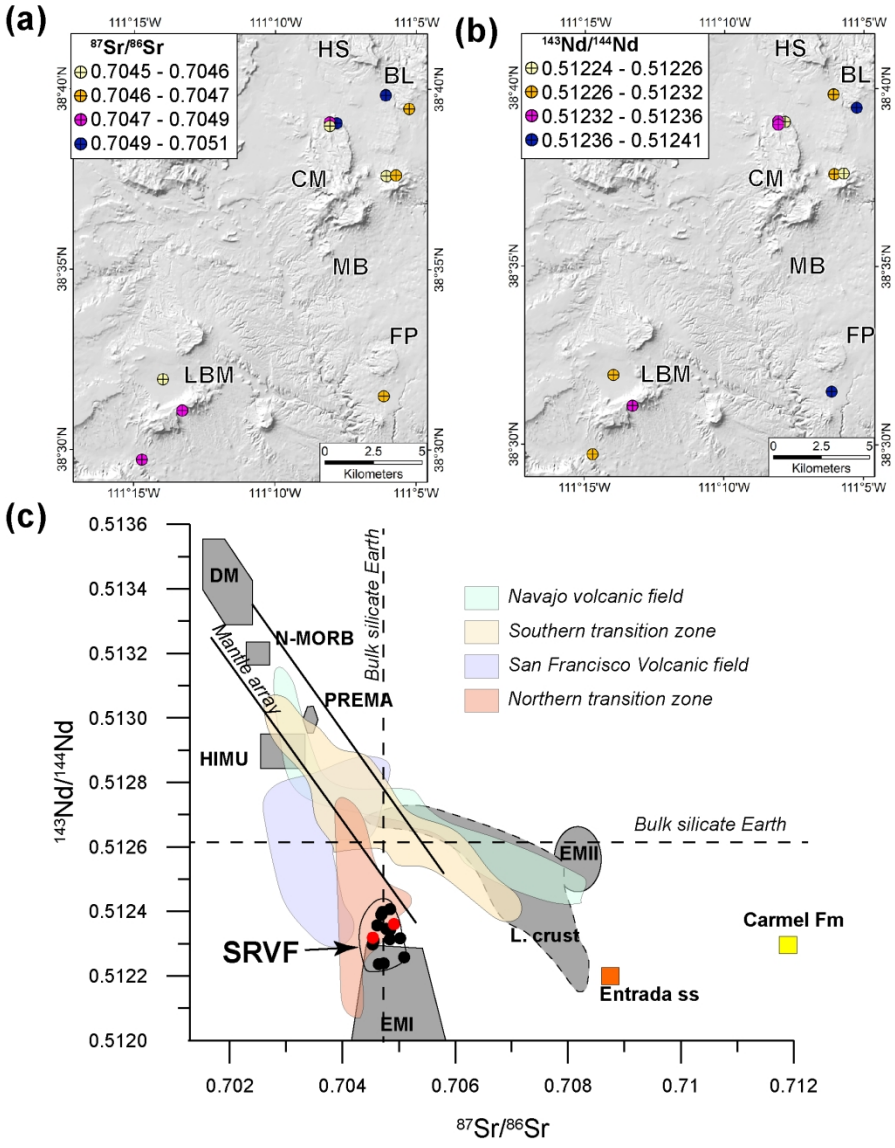

Figure 8: (a) Location of samples analyzed for 87Sr/86Sr and their isotopic ratio range. (b) Location of samples analyzed for 143Nd/144Nd and their isotopic ratio range. (c) 143Nd/144Nd versus 87Sr/86Sr diagram showing the relation of the SRVF igneous rocks (black and red circles for basalts and syenites, respectively, analytical error smaller than symbol size) to the mantle reservoirs as defined by Zindler and Hart (1986). Country rocks that contain the SRVF intrusions have been analyzed in this study and are also plotted: Entrada sandstone (orange square) and Curtis formation (yellow square). Bulk Silicate Earth values from Workman and Hart (2005). Also shown are the arrays defined by other volcanic fields of the transition zone between the Colorado Plateau and the Basin and Range province (Fig. 1), data downloaded from Georoc website (http://georoc.mpch-mainz.gwdg.de/) on 11/08/2019 and reported in supplementary table EA11: the Navajo volcanic field (Alibert et al., 1986; Roden et al., 1990; Kempton et al., 1991; Gibson et al., 1992), the Southern transition zone from Arizona to New Mexico (Alibert et al., 1986; Kempton et al., 1991; Crow et al., 2011), the San Francisco Volcanic field (Alibert et al., 1986; Bloomfield & Arculus, 1989; Kempton et al., 1991), and the northern transition zone in Utah (Reid & Ramos, 1996). Grey area for crust defined by data from Esperança et al., 1988.

FIGURE 9

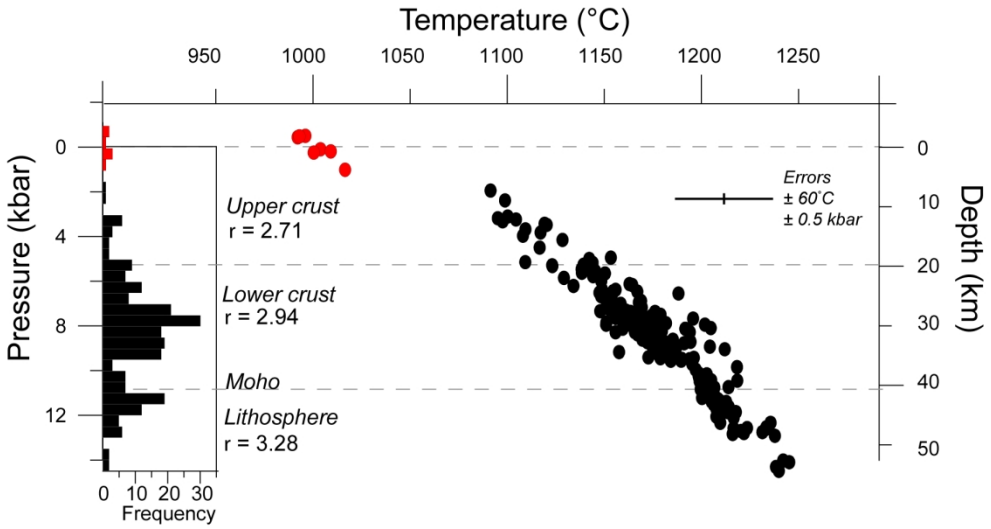

Figure 9: Temperature (°C) versus Pressure (kbar) and depth (km) from basalt (black) and syenite (red), calculated with the clinopyroxene-liquid thermobarometer of Putirka (2008) using clinopyroxene major element data and whole-rock major element compositions analyzed by EPMA and ICP-OES, respectively. Histogram of depths shows that basalt crystallizes over a broad range of pressures and temperatures as melts ascend through the lithosphere, with a majority of crystals forming between 30 and 22 km depth. Syenite crystallizes in the upper 4 km of the crust (Phanerozoic sediments) where intrusions have transitioned from dikes to sills (Richardson et al., 2015).

Figure 10

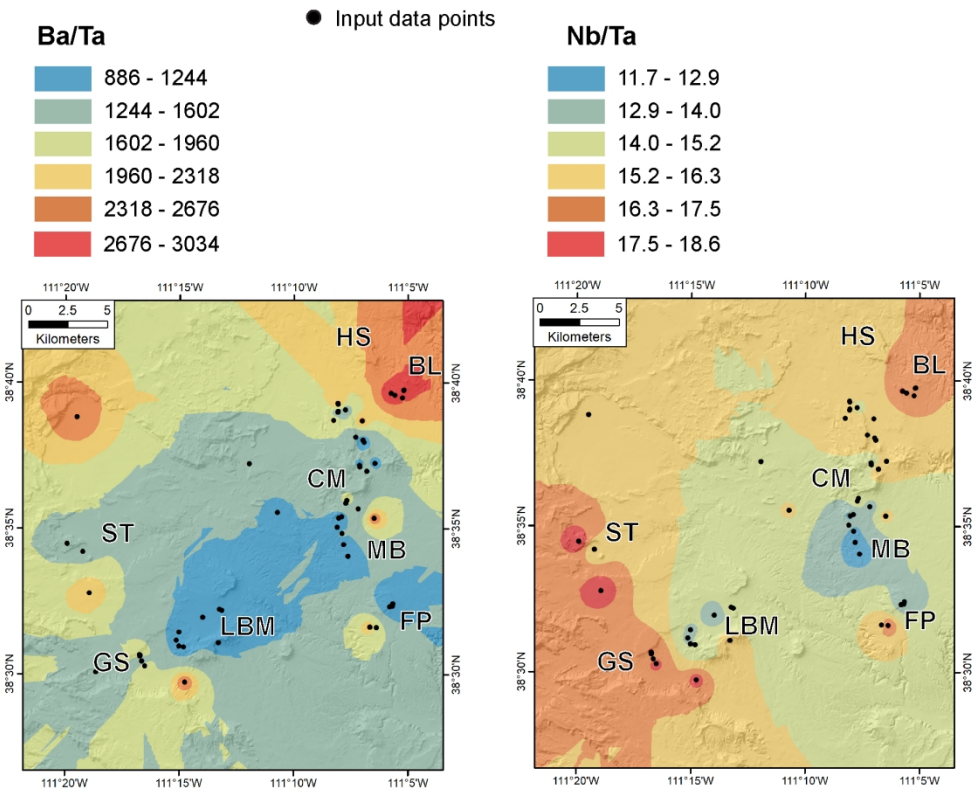

Figure 10: Geospatial distribution maps of trace element ratios in basalts obtained by Inverse Distance Weighting Interpolation in ArcGIS10. White circles show location of input data points. (a) ratio of Ba/Ta, (b) ratio of Nb/Ta.

FIGURE 11

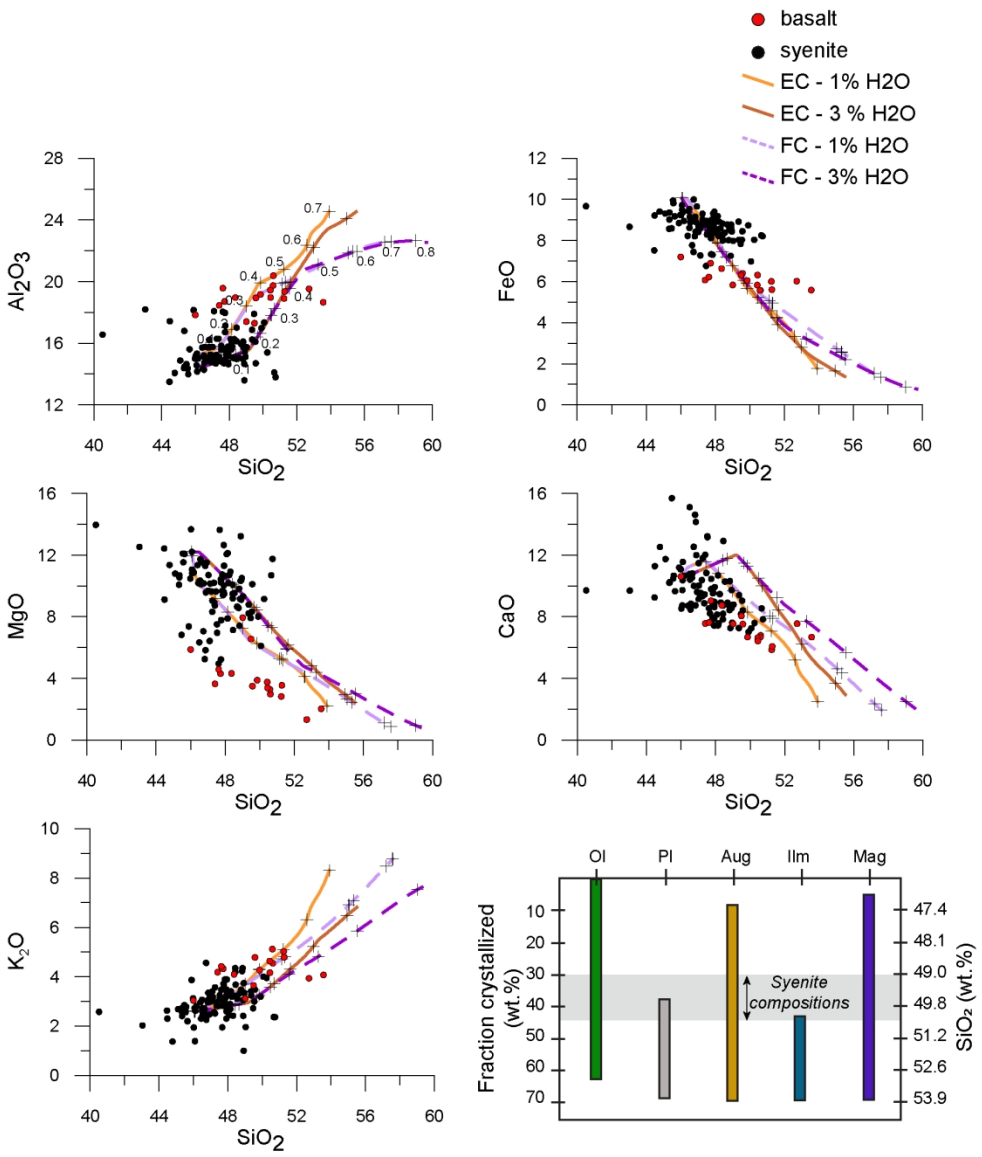

Figure 11: Representative major element modeling in COMAGMAT-3 program using CM-10 composition as initial liquid composition, and selecting decompression between 10 and 0.5 kbar, an open system with a QFM+1 oxygen buffer, and 1 – 3 wt. % of water. Equilibrium crystallization models are the bold orange lines. Fractional crystallization models are the dashed purple lines. Crosses are placed at 10% vol. crystallization intervals. Analytical error is smaller than symbol size.

FIGURE 12

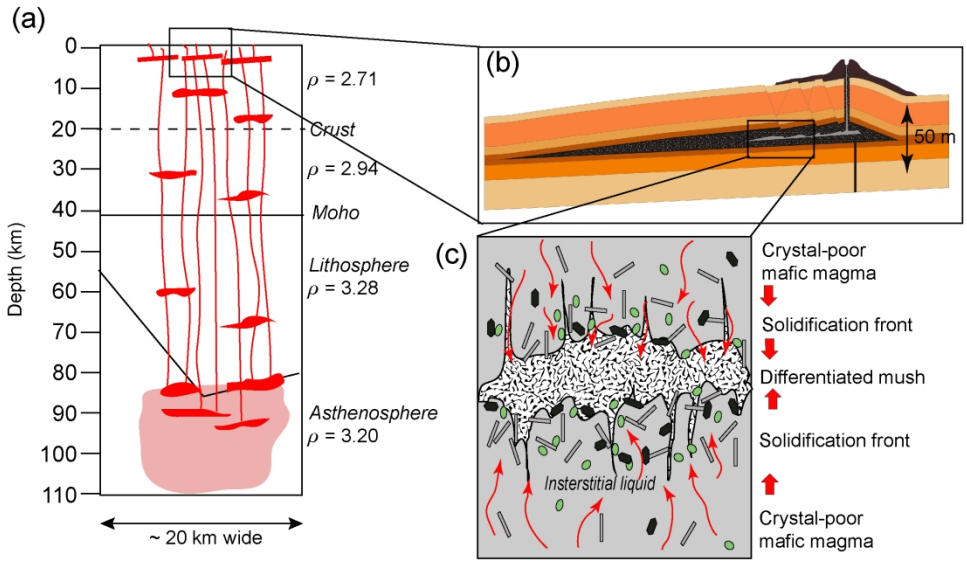

Figure 12: Conceptual model of the SRVF intrusions and magma differentiation by in-situ crystallization and progression of the solidification front. (a) SRVF melts ascend from the asthenosphere-lithosphere boundary then intruded the crust. Model of mantle and crust beneath the western transition zone of the Colorado Plateau adapted from Thompson & Zoback, 1979. (b) Sills intrude the San Rafael group, particularly the Entrada sandstone and Curtis formation, between 4 and 1 km below the surface. Sill thickness exaggerated to show segregation of syenite in basalt. (c) In-situ crystallization of basalt allows the formation and segregation of syenite by crystal mush compaction. The density contrast at relatively low viscosity allows syenite to percolate through the crystal mush and be remobilized into veins, lenses, and sheets.

Table 1: Isotopic data

Sample	rock type	Intrusive feature	Sr (ppm)	$^{87}Sr/^{86}Sr$	2σ	Nd (ppm)	$^{143}Nd/^{144}Nd$	2σ
BL-1	B	plug	1105	0.70469	0.000005	46.06	0.512390	0.000005
TT-4	B	plug	.	0.70464	0.000003	.	0.512237	0.000007
6-22-22	B	plug	.	0.70473	0.000005	.	0.512239	0.000004
CM-8	B	plug	.	0.70485	0.000002	.	0.512344	0.000004
6-20-22	B	plug	.	0.70509	0.000004	.	0.512258	0.000004
2-5-18	B	dyke	1265	0.70455	0.000008	59.02	0.512309	0.000004
TT-10	B	dyke	1625	0.70502	0.000005	63.58	0.512317	0.000004
6-21-22	B	dyke	.	0.70453	0.000035	.	0.512298	0.000004
FP-2	B	dyke	.	0.70471	0.000003	.	0.512399	0.000004
CM-10	B	sill	942	0.70462	0.000007	52.11	0.512357	0.000004
3-10-19	B	sill	883	0.70478	0.000005	48.14	0.512346	0.000007
4-13-20	B	sill	.	0.70484	0.000008	.	0.512314	0.000004
3-11-19a	B	sill	1234	0.70484	0.000006	52.23	0.512407	0.000007
3-9-19	SY	sill	.	0.70454	0.000006	.	0.512319	0.000007
3-11-19b	SY	sill	733	0.70491	0.000009	50.92	0.512361	0.000007
TT-11	Carmel Fm		229	0.71190	0.000005	28.72	0.512296	0.000005
entrada	Entrada ss		854	0.70875	0.000005	12.35	0.512200	0.000005

Table 2: Representative mineral mode in shonkinite and syenite. Detailed mode of individual samples can be found in supplemental EA1.

Rock type	Syenite	Basalt
crystallinity (vol.%)	100	10-70
Phenocrysts		
Olivine	0%	15 - 55 %
Pyroxene	10-30%	5 - 60 %
Plagioclase	15 - 20%	10 - 25 %
Sanidine	15 - 35%	<5%
Biotite	10-25%	5 - 15%
Amphibole	10-25%	<15%
Magnetite	<15%	<15%
Grain size (mm)	0.5 - 50	0.2 - 2
Groundmass		
Olivine	n.a.	10%
Pyroxene	n.a.	20%
plagioclase	n.a.	25%
Biotite	n.a.	<10%
Magnetite	n.a.	20%
Glass	n.a.	<5%